A phase field approach to fracture for hyperelastic and visco-hyperelastic materials applied to pre-stressed cylindrical structures

A. Valverde-González [a,b], J. Reinoso [b], N. K. Jha [c], J. Merodio [c] and M. Paggi [a]

[a]IMT School for Advanced Studies, Piazza San Francesco 19, Lucca 55100, Italy;
[b]Departamento de Mecánica de Medios Continuos y Teoría de Estructuras, Escuela Técnica Superior de Ingeniería, Universidad de Sevilla, Camino de los Descubrimientos s/n, 41092, Sevilla, Spain; [c]Departamento de Matemática Aplicada a las TIC, ETS de Ingeniería de Sistemas Informáticos, Universidad Politécnica de Madrid, Madrid, 28031, Spain

ABSTRACT
In this investigation, the mechanical modeling of nonlinear visco-hyperelastic residually stressed materials obtained from an invariant-based constitutive energy framework is coupled with the phase field approach to fracture. The main target regards the extension of the phase-field method to simulate pre-stressed cylindrical structures subjected to monotonic axial pulling load upon failure. This formulation is incorporated into a numerical procedure using the Finite Element Method (FEM), in particular, it is implemented in the commercial FE package `ABAQUS` as a user subroutine `UMAT`. Results suggest the dependence of the mechanical behavior and the crack pattern of these structures on not only viscous parameters like the relaxation time and the displacement rate, but also on the strength of the residual stress field, which in turn depends on geometrical characteristics of the cylindrical structure such as the radius or the length. A range of solutions related to crack propagation is shown for different cylindrical structures, from azimuthal crack propagation to axial one. The proposed framework aims to provide an extended application for the already-defined visco-hyperelastic formulation by the inclusion of residual stresses.

1. Introduction

Cylindrical structures (tube mechanics) are elements of considerable interest in applications concerning rubber-like materials and soft tissues and can be categorized as either thin or thick-walled structures. Complying with this structural feature, the existence of residual stresses within the body does affect its mechanical behavior. Residual stresses are associated with different processes used to manufacture materials [1] as well as with living tissues growth [2], among other areas. Specifically, within the biomechanics field, residual stresses can be revealed by cutting (closed and unloaded) axial segments of arteries since they deform when they are slit [3]. It is well known that

---

CONTACT A. Valverde-González. Email: angel.valverde@imtlucca.it

residual stresses play an important role in the biological process of homeostasis, which is the state of steady internal, physical and chemical conditions maintained during optimal functioning by living systems [4]. A matter of upmost important to the scientific community (with a clear benefit for the society) is the role that residual stresses, and other factors, play in the understanding of arterial failure. From the mechanical standpoint, arterial failure is affected by bulging- and bending-related instabilities of inflated and extended tubes. These aspects have been lately investigated within the context of aneurysms formation and rupture caused by high blood pressure and weakening of the artery wall [5–8].

In order to analyze, mitigate and potentially prevent failure of pre-stressed cylindrical structures, the development of a rigorous and sophisticated theoretical analysis is required. This is usually complemented with the advent of reliable numerical techniques to obtain a general modelling framework that allows qualitatively and quantitatively different aspects such as the nonlinear behavior of (visco-hyperelastic) materials to be considered [9]. This constitutive material model is often related to its microstructure including a network of highly flexible and mobile chains which are three dimensional cross linked. Particularly, in polymers, the movement of the chains is associated with viscous effects occurring in the rubber-like material, see [10] and references therein. Moreover, as reported in [11], in materials prone to experience viscous effects, the principal failure mechanism of a considerable number of elastomers is strongly affected by the inelastic term and the rate of deformation. Accordingly, several rheological models have been developed to describe the viscoelastic constitutive law for elastomers which can be split into linear [12–16] and non-linear viscoelasticity [17–19].

Within failure analysis of cracking events, fracture in elastomer-like materials is often related to either nucleation of cavities (cavitation) [20] or crack propagation. The latter is the focus of this work and a macromechanics approach is pursued. In the literature, several methods have been proposed to model fracture for hyperelastic materials [21]. These methods include fracture mechanics-based methodologies [22, 23], path-independent J-integral formulations [24–26], cohesive methods [27, 28] and peridynamical approaches [29, 30], among others. Recently, the phase field approach to fracture has emerged as a new modelling technique to simulate rate-dependent fracture evolution. Based on the classical brittle fracture theory given by [31] (which defined the crack growth when the energy release rate $\mathcal{G}$ reaches its critical value $\mathcal{G}_C$), Francfort and Marigo [32] incorporated the phase field approach to formulate brittle fracture and Bourdin and co-authors. [33] proposed the phase-field regularization of fracture as an energy minimization problem of the fracture energy and the strain energy potential. In addition to brittle fracture [34–37], the phase field technique has been extended to ductile fracture [38–44], anisotropic fracture [45–51], dynamic fracture [52–54], and failure of heterogeneous media [55–60]. It is also worth mentioning the breakthrough implementation of the technique of phase field using Deep Neural Networks carried out in [61]. In addition to this, some few approaches have been proposed to simulate fracture phenomena in visco-elastic materials [62–66], along with another nonlocal damage techniques like the element failure method [67, 68].

The first objective of this paper is, by employing the current visco-hyperelastic theory, to formulate a phase field model able to capture fracture events in hyperelastic and visco-elastic solids, a topic broadly covered as has been aforementioned. Once this framework is implemented, the salient novelty of the present research is the subsequent incorporation of residual stresses in order to model fracture for pre-stressed cylindrical structures, being this combined modelling the main aim of the paper. For that last

2

purpose, we use a constitutive law for residually stressed hyperelastic materials given in terms of invariants, see [69–74].

In order to tackle the targets of this work, the phase field approach for visco-elastic fracture proposed by [64] is combined with the rheological approach given in [10]. Accordingly, a new model is generated enabling the investigation fracture phenomena for elastomers with viscous response. Furthermore, the model is extended to simulate pre-stressed cylindrical structures using the constitutive framework proposed in [69]. The viscoelastic effect and the residual stresses are defined separately and are added subsequently to give the total energy driving force of the system complying with thermodynamic restrictions and establishing the corresponding modular format of the theoretical framework.

The article is structured as follows. The formulation, which consists in the hyperelastic viscoelastic material law at hand, is developed in Sec. 2. The phase-field governing functional along with its computational implementation in an `UMAT` subroutine is presented in Sec. 3. A benchmark example is carried out in Sec. 4.1 to verify the hyper-visco elastic formulation. Cylindrical structures are simulated in Sec. 4.2 where a deep parametric study is carried out for viscosity-dependent parameters such as relaxation time and displacement rate and for different residual stress fields. Since many vanguard technologies are employing multi-layered structures with different mechanical and fracture properties [75, 76], in Sec. 4.3, the analysis of a two-layer hollow thick-walled cylinder is executed to address the dependence of shear modulus mismatch between the layers, as well as fracture energy mismatch, and the presence of pre-stresses on the mechanical performance of this structural element. Some final remarks and conclusions are provided in Sec. 5.

2. Governing equations and constitutive formulation

This section outlines the fundamental concepts and definitions for hyperelastic and visco-hyperelastic solids within the scope of the phase field approach to fracture.

2.1. Basic definitions

Complying with standard nonlinear Continuum Mechanics, the reference configuration of an arbitrary body is denoted by $\Omega_0 \subset \mathbb{R}^n$, being the arbitrary material points in the reference placement denoted by the vector $\mathbf{X}$. Throughout the deformation process this reference configuration is mapped at an arbitrary elapsed time t, with $\mathcal{T} = [0, t]$ onto the corresponding current configuration $\Omega \subset \mathbb{R}^n$ whose position vectors are identified by the vector $\mathbf{x}(\mathbf{X}, t)$

The mapping of the material positions from the initial to the current configuration is ruled by the non-linear deformation map $\boldsymbol{\varphi}(\mathbf{X}, t)$, with $\mathbf{x} := \boldsymbol{\varphi}(\mathbf{X}, t)$. This transformation is shown in Fig. 1. The deformation of the body is described by the deformation gradient $\mathbf{F}$, which is used to linearly map tangent vectors from the initial to the current configuration:

$$\mathbf{F} := \nabla_{\mathbf{X}} \boldsymbol{\varphi}(\mathbf{X}, t) = \mathbf{1} + \mathbf{H}(\mathbf{X}, t) \tag{1}$$

where $\mathbf{1}$ is the second order identity tensor and $\mathbf{H}(\mathbf{X}, t)$ is identified with the material displacement gradient tensor. The determinant of $\mathbf{F}$ that is denoted by J should fulfill
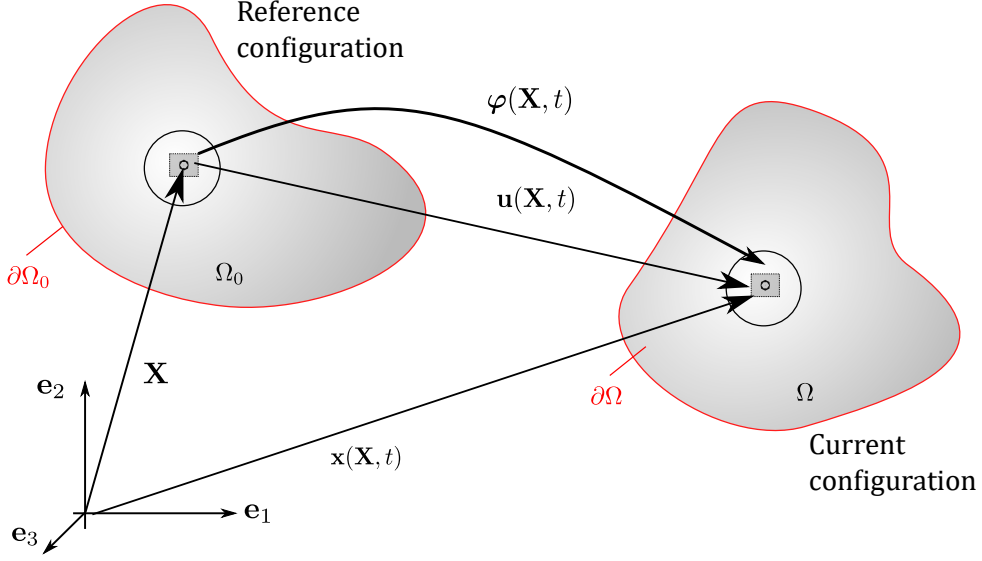
3

Figure 1. Deformation process from the reference configuration to the current one.

the condition $J = \det[\mathbf{F}] \geq 0$.

The displacement vector is introduced to describe the motion of the body from the reference to the current configuration at time t in Eq. (2), tracking the current position of the material points from the reference state:

$$\mathbf{u}(\mathbf{X}, t) := \mathbf{x}(\mathbf{X}, t) - \mathbf{X} \tag{2}$$

From this, the right and left Cauchy-Green tensors are respectively obtained as

$$\mathbf{C} := \mathbf{F}^{\mathrm{T}}\mathbf{F}; \quad \mathbf{b} := \mathbf{F}\mathbf{F}^{\mathrm{T}} \tag{3}$$

Crack events in the proposed modelling framework are accounted for the consideration of the phase field approach [33, 77]. The crack-phase field variable is described via the material variable $\mathfrak{d}(\mathbf{X}, t)$:

$$\mathfrak{d}(\mathbf{X}, t) : \Omega_0 \times \mathcal{T} \to [0, 1] \tag{4}$$

where the state $\mathfrak{d}(\mathbf{X}, t) = 0$ identifies an intact stiffness at the material point level, whereas $\mathfrak{d}(\mathbf{X}, t) = 1$ denotes a fully deteriorated stiffness. This variable recalls the level set of the crack in the reference configuration, see Fig. 2. The phase field method is characterized by a regularization parameter ℓ that smears out the sharp crack by a diffusive crack topology within a regularization region.

2.2. Constitutive formulation

With regard to the constitutive formulation, this subsection presents the particular visco-hyperlasticity model adopted from [10]. This formulation relies on the considera-
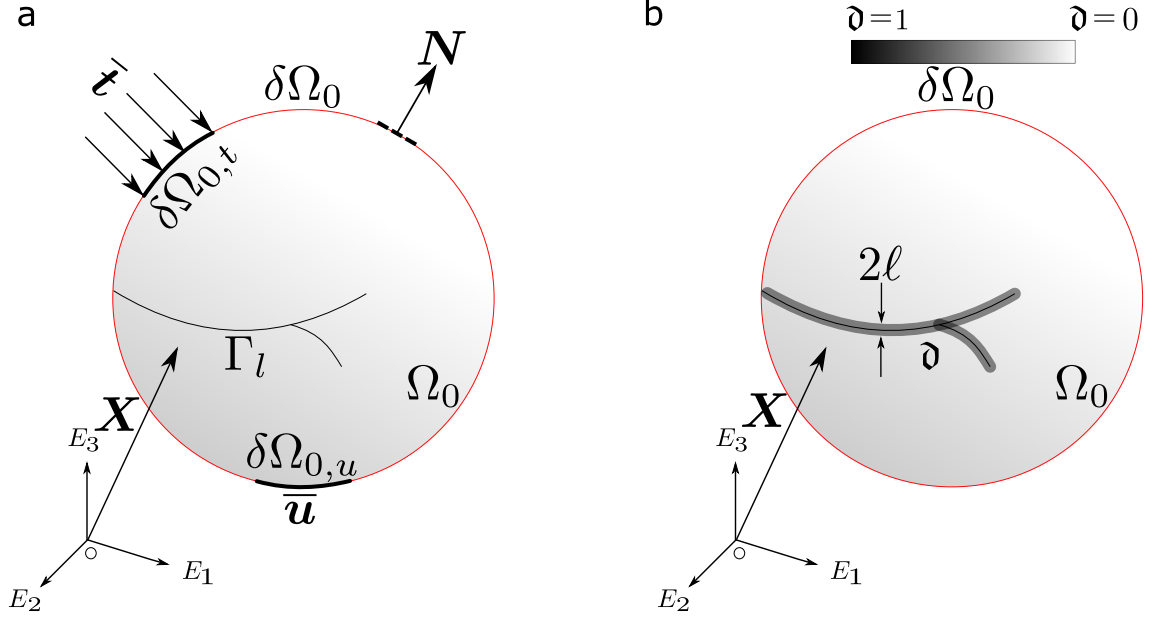
4

Figure 2. Phase field approximation of a sharp crack discontinuity in a deformable body in the reference configuration. (a) sharp crack representation, (b) regularized crack representation in the spirit of the phase field approach of fracture.

tion of its microstructure (highly mobile and flexible macro-molecules). The resulting constitutive equations of rubber viscoelasticity are obtained under the assumption of the polymer microstructure behaving like several idealized polymer networks. This mechanical response is characterized by macromolecules which are strongly cross-linked in a network, where there is a sub-network with highly mobile and temporary entanglement mechanisms. The cross-linking is related to the elastic response, whereas the subnetwork is responsible for the viscous behaviour. The macroscopic representation of the system is seen in Fig. 3. Following this definition, the macroscopic finite rubber response can be defined based on a volumetric-isochoric decomposition, where the latter part itself is decomposed into an elastic and a viscous term, respectively.

Concerning the incorporation of residual stresses, a nonlinear constitutive law that depends on a number of invariants is considered recalling the original framework developed in [69, 78]. This formulation presents the following advantages: (i) it can be implemented into standard FE codes in a straightforward manner, (ii) it can be combined with different kinds of mechanical problems, and (iii) it precludes the use of the multiplicative descomposition as is proposed in [79]. With these arguments, the Helmholtz free energy function $\Psi(\mathbf{C}, \mathbf{A}, \boldsymbol{\sigma_0})$ is postulated as follows:

$$\Psi(\mathbf{C}, \mathbf{A}, \boldsymbol{\sigma_0}) = \Psi^{\mathrm{hyp}}(\mathbf{C}) + \sum_{\alpha=1}^{\mathrm{n}} \Psi^{\mathrm{visco},\alpha}(\mathbf{C}, \mathbf{A}) + \Psi^{\mathrm{res}}(\mathbf{C}, \boldsymbol{\sigma_0}) \tag{5}$$

where we have the expression for the free energy divided in three terms associated to the main features of the model: (i) Ψ^{hyp}, related to the hyperelastic constitutive part; (ii) $\Psi^{\mathrm{visco},\alpha}$, dedicated to every α viscous branch; and (iii) Ψ^{res}, referred to the residual stresses present in the model. n makes reference to the number of viscous terms considered in the rheological model; $\mathbf{A}$, to the tensor that considers the stretches $\boldsymbol{\lambda}$ from the microscopical system of polymer chains; and $\boldsymbol{\sigma_0}$, to the residual stress field
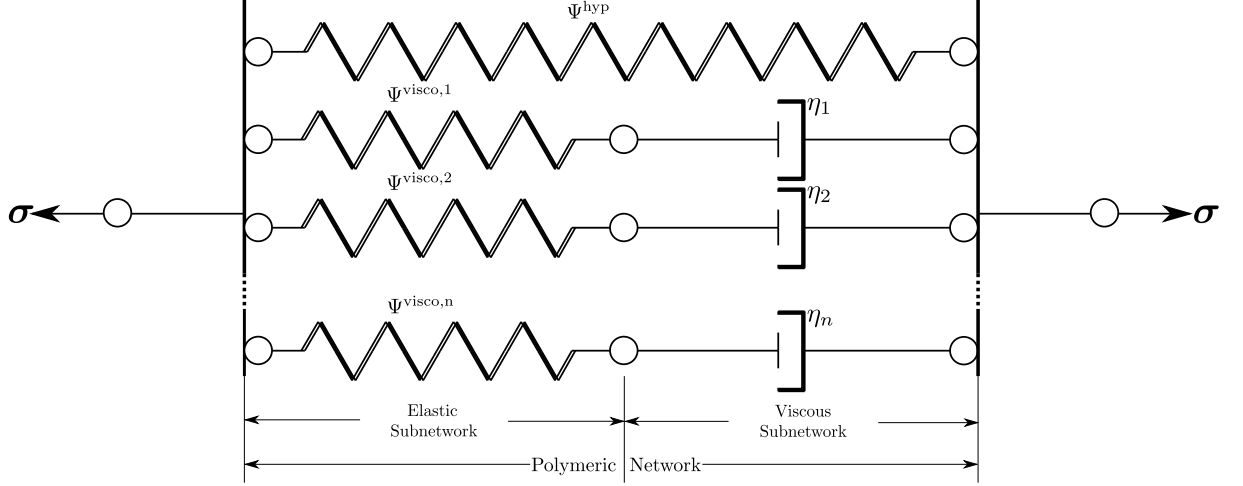
Figure 3. Maxwellian rheological model of the response of the material consisting of the elastic branches, representing the strongly cross-linked network, and the viscous branches, representing the highly mobile with entanglements subnetwork.

in the reference configuration.

First, focusing on the hyperelastic term, Ψ^{hyp}, this also can be split into the corresponding volumetric (Ψ^{vol}) and isochoric (Ψ^{iso}) contributions:

$$\Psi^{\mathrm{hyp}}(\mathbf{C}) = \Psi^{\mathrm{iso}} + \Psi^{\mathrm{vol}} \tag{6}$$

which can be specialized to a standard neo-Hookean model:

$$\Psi^{\mathrm{iso}} = \frac{\mu}{2}(\bar{I}_1 - 3), \quad \Psi^{\mathrm{vol}} = \frac{\kappa}{2}(J - 1)^2 \tag{7}$$

where μ and κ denote the shear and the volumetric constant, respectively; and $\bar{I}_1$ is the first invariant of the deviatoric left Cauchy-Green tensor which has the value of $\bar{I}_1 = J^{-2/3}I_1 = J^{-2/3}\mathrm{tr}[\mathbf{C}]$.

The second Piola-Kirchhoff stress for the hyperelastic term $\mathbf{S}^{\mathrm{hyp}}$ is evaluated as:

$$\mathbf{S}^{\mathrm{hyp}} := 2\frac{\partial \Psi^{\mathrm{hyp}}}{\partial \mathbf{C}} = 2J^{-2/3}\mu\left(\mathbf{I} - \frac{I_1 \mathbf{C}^{-1}}{3}\right) \tag{8}$$

For the second term in Eq. (5), the viscous part of the model, Ψ^{visco}, and the corresponding second Piola-Kirchhoff viscous overstress, $\mathbf{S}^{\mathrm{visco}}$, is particularized without any loss of generality to the model proposed by Linder and co-authors [10]. In this work, it is observed how the visco-elastic contribution is constructed from the microscopical description of the polymer chains movement, being this microscopic-based approach embedded into the current continuous framework of finite rubber viscoelasticity. The temporary state of such system of polymer chains is measured by a probability function $p(\boldsymbol{\lambda}, t)$ obtained from the diffusion process. This magnitude is dependent from the stretch state of the chain $\boldsymbol{\lambda}$. By representing this probability function in a tensorial form, we can associate a stretch space $\mathcal{L}_{\mathbf{x}}$ connected locally to a material point with position $\mathbf{x}$ in the current configuration $\Omega \subset \mathbb{R}^n$ and map his evolution from the initial

stretch space $\mathcal{L}_\mathbf{X}$, linked to a material point with position $\mathbf{X}$ in the reference configuration $\Omega_0 \subset \mathbb{R}^n$, by means of the microdeformation map $\bar{\mathbf{P}}$. More particular details are omitted here for the sake of brevity and the reader is referred to [10]. Recalling this constitutive model, via the definition of a so-called microdeformation map $\bar{\mathbf{P}}$, it is possible to account for the micromechanics of the system by defining:

$$\bar{\mathbf{P}} = \bar{\mathbf{F}}\bar{\mathbf{P}}_\mathbf{X} \tag{9}$$

where $\bar{\mathbf{P}}_\mathbf{X}$ stands for the pre-deformation map tensor, and $\bar{\mathbf{F}}$ is the isochoric part of the deformation gradient at the macroscopic level.

After some operations, one reaches the definition of the tensor $\mathbf{A}$

$$\mathbf{A} = \bar{\mathbf{P}}_\mathbf{X}\bar{\mathbf{P}}_\mathbf{X}^\mathrm{T}. \tag{10}$$

Note that the tensor $\mathbf{A}$ provides the information concerning the microdeformation of the visco-elastic subnetwork in the initial configuration and it depends on macroscopic variables. Accordingly, the time evolution equation of this tensor reads

$$\dot{\mathbf{A}} = \frac{1}{\tau^\alpha}(\bar{\mathbf{C}}^{-1} - \mathbf{A}) \tag{11}$$

where $\bar{\mathbf{C}}^{-1}$ is the inverse of the isochoric part of the right Cauchy-Green tensor, and τ^α, the relaxation time associated to the viscous mechanism α.

After the previous definitions, the viscous counterpart of the free energy density is obtained for every α polymer chain network

$$\Psi^{\mathrm{visco},\alpha}(\mathbf{C}, \mathbf{A}) = \frac{1}{2}\mu^{\mathrm{visco},\alpha}[(\mathbf{A}^{(\alpha)} : \bar{\mathbf{C}}) - \ln(\det\mathbf{A}^{(\alpha)})] \tag{12}$$

being $\mu^{\mathrm{visco},\alpha}$ the shear modulus for each mechanism.

After some algebraic manipulations, the resulting closed form expression for the viscous part of the hyperelastic energy allows the computation of the second Piola-Kirchhoff viscous overstress tensor $\mathbf{S}^{(\mathrm{visco},\alpha)}$ for each α mechanism, which reads

$$\mathbf{S}^{(\mathrm{visco},\alpha)} = J^{-2/3}\mathbb{P} : \left(\mu^{\mathrm{visco},\alpha}\mathbf{A}^{(\alpha)}\right) \tag{13}$$

where $\mathbb{P}$ is the fourth-order projector operator

$$\mathbb{P} : (\bullet) = \bullet - \frac{1}{3}[(\bullet) : \mathbf{C}]\mathbf{C}^{-1}. \tag{14}$$

Regarding the last term, associated with residual stresses, Ψ^{res}, in Eq. (5), a few assumptions are made about the particular form of the stress field $\boldsymbol{\sigma_0}$ that is defined in the reference configuration. Following [69], this stress field is assumed to be symmetric, and fulfilling the conditions:

7

$$\text{div } \boldsymbol{\sigma_0} = \mathbf{0} \text{ in } \Omega_0, \tag{15}$$

$$\boldsymbol{\sigma_0}\mathbf{N} = \mathbf{0} \text{ on } \partial\Omega_{0,t} \tag{16}$$

where $\mathbf{N}$ is the normal vector to the boundary in the reference configuration. Exploiting the previous assumptions, the particular form of $\Psi^{\text{res}}(\mathbf{C}, \boldsymbol{\sigma_0})$ is given by

$$\Psi^{\text{res}}(\mathbf{C}, \boldsymbol{\sigma_0}) = \frac{f}{2}(I_5 - \text{tr}\boldsymbol{\sigma_0}) + \frac{1-f}{4}(I_6 - \text{tr}\boldsymbol{\sigma_0}) \tag{17}$$

where $I_5 = \text{tr}(\boldsymbol{\sigma_0}\mathbf{C})$ and $I_6 = \text{tr}(\boldsymbol{\sigma_0}\mathbf{C}^2)$ are the invariants associated with the residual stress field and f is a parameter that accounts for the weight of these invariants in the equation. As this is a nonlinear problem, the residual stresses are necessarily nonuniform and geometrically dependent, and the elastic response of the system will be in-homogeneous [70].

For the subsequent numerical implementation, the contribution of the residual stresses to the Second Piola-Kirchhoff stress is computed as:

$$\mathbf{S}^{\text{res}} = 2\frac{\partial\Psi^{\text{res}}}{\partial\mathbf{C}} = 2J^{-1/3}\left(\frac{f\boldsymbol{\sigma_0}}{2} - \frac{fI_5\mathbf{C}^{-1}}{6}\right) + (1-f)J^{-2/3}\left(\frac{1}{4}\frac{\partial I_6}{\partial\mathbf{C}} - \frac{I_6\mathbf{C}^{-1}}{6}\right). \tag{18}$$

where we have needed the forthcoming expressions to account for the derivative $\frac{\partial\Psi^{\text{res}}}{\partial\mathbf{C}}$

$$\frac{\partial I_5}{\partial\mathbf{C}} = \boldsymbol{\sigma_0}, \quad \frac{\partial I_6}{\partial\mathbf{C}} = \boldsymbol{\sigma_0}\mathbf{C} + \mathbf{C}\boldsymbol{\sigma_0} \tag{19}$$

Considering Eqs. (8), (13) and (18), one reaches the complete form of total second Piola-Kirchhoff stresses herein proposed:

$$\mathbf{S} = \mathbf{S}^{\text{hyp}} + \sum_{\alpha=1}^{n}\mathbf{S}^{\text{visco},\alpha} + \mathbf{S}^{\text{res}}. \tag{20}$$

3. Governing functional and implementation details

3.1. Governing functional

The governing functional of the phase field approach to fracture (governing crack nucleation, propagation and branching) is recalled by the definition of the corresponding energy functional [34, 80]. In line with the ideas of [32], we define the energy functional $\Pi(\mathbf{u}, \Gamma)$ of the system in the reference configuration as:

$$\Pi(\mathbf{u}, \Gamma) = \Pi_\Omega(\mathbf{u}, \Gamma) + \Pi_\Gamma(\Gamma) = \int_{\Omega_0}\Psi(\mathbf{C}, \mathbf{A}, \boldsymbol{\sigma_0}, \mathfrak{d})\text{d}\Omega_0 + \int_{\Omega_0}\mathcal{G}_C\gamma(\mathfrak{d}, \nabla_\mathbf{X}\mathfrak{d})\text{d}\Omega_0 \tag{21}$$

where $\Psi(\mathbf{C}, \mathbf{A}, \boldsymbol{\sigma_0}, \mathfrak{d})$ refers to the expression defined in Eq. (5), $\mathcal{G}_C$ stands for the fracture energy (independent of viscoelastic parameters); and γ is the crack energy density functional. There are two different terms in Eq. (21), being $\Pi_\Omega(\mathbf{u}, \Gamma)$ the one that represents the energy stored in the solid and $\Pi_\Gamma(\Gamma)$, the energy necessary to create the crack according to Griffith theory.

Without loss of generality, the driving force for damage evolution is assumed to be driven by the free energy function stated above, $\Psi(\mathbf{C}, \mathbf{A}, \boldsymbol{\sigma_0}, \mathfrak{d})$. Therefore, upon the occurrence of cracking events, we postulate a degradation function $g(\mathfrak{d})$ affecting to $\Psi(\mathbf{C}, \mathbf{A}, \boldsymbol{\sigma_0})$: $\Psi(\mathbf{C}, \mathbf{A}, \boldsymbol{\sigma_0}, \mathfrak{d}) = g(\mathfrak{d})\Psi(\mathbf{C}, \mathbf{A}, \boldsymbol{\sigma_0})$.

Moreover, in order to prevent self-healing at the material point level, the engineering formulation proposed by Miehe and co-authors [34] is used. This formulation assumes a time-dependent t history variable parameter $\mathcal{H}$:

$$\mathcal{H} = \max_{t \in [0, t_f]} \Psi(\mathbf{C}, \mathbf{A}, \boldsymbol{\sigma_0}, t). \tag{22}$$

The so-called crack density functional defined above, $\gamma(\mathfrak{d}, \nabla_\mathbf{X}\mathfrak{d})$, depends upon the length-scale parameter ℓ and the continuous scalar-valued phase field variable $\mathfrak{d}$. In line with [34], a possible choice for $\gamma(\mathfrak{d}, \nabla_\mathbf{x}\mathfrak{d})$ renders

$$\gamma(\mathfrak{d}, \nabla_\mathbf{X}\mathfrak{d}) = \frac{1}{4c_w}\left(\frac{1}{\ell}w(\mathfrak{d}) + \ell|\nabla_\mathbf{X}\mathfrak{d}|^2\right) \tag{23}$$

where $w(\mathfrak{d})$ is the geometric crack function and c_w is a parameter, which, like the previous one, depends on the applied phase field approach and determines the dissipation function.

It is important to remark the necessity to propose a formulation where crack growth only accounts while in a tension state. Therefore, to distinguish these states, we will consider the approach proposed by Borden and co-authors [40]. In here, there is a decomposition of the elastic strain energy density Ψ to distinguish between tensile Ψ^+ and compressive states Ψ^-. With these ingredients at hand, Eq. (21) is reformulated as:

$$\begin{aligned}\Pi(\mathbf{u}, \mathfrak{d}) &= \int_{\Omega_0} [g(\mathfrak{d})\Psi^+(\mathbf{C}, \mathbf{A}, \boldsymbol{\sigma_0}, J) + \Psi^-(J)]\mathrm{d}\Omega_0 \\ &+ \int_{\Omega_0} \frac{\mathcal{G}_C}{4c_w}\left(\frac{1}{\ell}w(\mathfrak{d}) + \ell|\nabla_\mathbf{X}\mathfrak{d}|^2\right)\mathrm{d}\Omega_0.\end{aligned} \tag{24}$$

In order to define the tensile and compressive states for the strain energy density, we employ the isochoric-volumetric decomposition of Amor and co-authors [81]:

$$\Psi^+(\mathbf{C}, \mathbf{A}, \boldsymbol{\sigma_0}, J) = \begin{cases} \Psi^{\mathrm{hyp}}(\mathbf{C}) + \sum_{\alpha=1}^n \Psi^{\mathrm{visco},\alpha}(\mathbf{C}, \mathbf{A}) + \Psi^{\mathrm{res}}(\mathbf{C}, \boldsymbol{\sigma_0}) & \text{if } J \geq 1 \\ \Psi^{\mathrm{iso}}(\mathbf{C}) + \sum_{\alpha=1}^n \Psi^{\mathrm{visco},\alpha}(\mathbf{C}, \mathbf{A}) + \Psi^{\mathrm{res}}(\mathbf{C}, \boldsymbol{\sigma_0}) & \text{if } J < 1 \end{cases} \tag{25}$$

$$\Psi^-(J) = \begin{cases} 0 & \text{if } J \geq 1 \\ \Psi^{\mathrm{vol}}(J) & \text{if } J < 1 \end{cases} \tag{26}$$

9

where the expressions for the isochoric Ψ^{iso} and the volumetric Ψ^{vol} can be found in Eq. (7).

Therefore, as the degradation function only multiplies the positive cases Ψ^+, the history field variable is defined upon them $\mathcal{H}^+$.

$$\mathcal{H}^+ = \max_{t\in[0,t_f]}\Psi^+(\mathbf{C}, \mathbf{A}, \boldsymbol{\sigma_0}, t). \tag{27}$$

For the particularization to the so-called AT2 model [33], the degradation function is formulated using a quadratic function:

$$g(\mathfrak{d}) = (1 - \mathfrak{d})^2 + \mathcal{K} \tag{28}$$

being $\mathcal{K}$ a parameter of residual stiffness which avoids, at the same time, the system to become ill-conditioned with numerical instabilities. For the dissipation conditions of AT2, we set $w(\mathfrak{d}) = \mathfrak{d}^2$ and $c_w = \frac{1}{2}$.

The solution of Eq. (28) can be obtained by solving it as a minimization problem.

$$\boxed{\begin{array}{ll} \text{Determine} & (\mathbf{u}, \mathfrak{d}) \quad \text{from} \\ (\mathbf{u}^*, \mathfrak{d}^*) = \arg\min\limits_{\mathcal{S}} \Pi(\mathbf{u}, \mathfrak{d}), \end{array}} \tag{29}$$

with $\mathcal{S} = \{\dot{\mathfrak{d}} \geq 0 \text{ for all } \mathbf{X} \in \Omega_0\}$.

Following a standard Galerkin procedure, the weak form of the coupled displacement $\mathbf{u}$ and fracture problem $\mathfrak{d}$ in Eq. (24) can be obtained as:

$$\delta\Pi(\mathbf{u}, \delta\mathbf{u}, \mathfrak{d}, \delta\mathfrak{d}) = \underbrace{\int_{\Omega_0} \mathbf{S} : \delta\mathbf{E}\mathrm{d}\Omega_0}_{\delta\Pi_{\mathrm{int}}^{\mathbf{u}}} -$$

$$\underbrace{\int_{\Omega_0} [g'(\mathfrak{d})(\delta\mathfrak{d})\Psi^+]\mathrm{d}\Omega_0 + \int_{\Omega_0} \mathcal{G}_C\ell\left[\frac{\mathfrak{d}}{\ell^2}\delta\mathfrak{d} + \nabla_{\mathbf{X}}\mathfrak{d} \cdot \nabla_{\mathbf{X}}(\delta\mathfrak{d})\right]\mathrm{d}\Omega_0}_{\delta\Pi_{\mathrm{int}}^{\mathfrak{d}}}. \tag{30}$$

where $\mathbf{E}$ refers to the Green-Lagrange strain tensor, which reads as $\mathbf{E} = \frac{1}{2}(\mathbf{C} - \mathbf{1})$, being 1 the identity matrix. Upon the exploitation of the product rule and the Gauss' divergence theory on Eq. (30), the phase field evolution equation is obtained as

$$-2(1 - \mathfrak{d})\underbrace{\Psi^+(\mathbf{C}, \mathbf{A}, \boldsymbol{\sigma_0})}_{\mathcal{H}^+} + \mathcal{G}_C\left(\frac{1}{\ell} - \ell\nabla^2\mathfrak{d}\right) = 0. \tag{31}$$

Despite the robustness of the proposed formulation, convergence issues may arise due to local instabilities. Therefore, according to [64], a pseudo-viscous resistance against phase field evolution χ is added as a positive viscous damping term. This is a parameter is employed in order to increase the numerical stability and to account for the results of quasi-brittle fracture, which are obtained for $\chi = 0$. By increasing χ,

the fracture gets delayed compared to brittle fracture. However, χ should be kept as a very small number, since large values of this parameter leads to numerical instabilities in achieving equilibrum solutions. The term is added to Eq. (31) and it yields

$$-2(1-\mathfrak{d}) \underbrace{\Psi^+(\mathbf{C},\mathbf{A},\boldsymbol{\sigma_0})}_{\mathcal{H}^+} +\mathcal{G}_C\left(\frac{1}{\ell}-\ell\nabla^2\mathfrak{d}\right) + \chi\dot{\mathfrak{d}} = 0. \qquad (32)$$

3.2. Implementation details

This section briefly describes the numerical implementation of the current phase field model for hyperelastic (rate independent) and visco-hyperelastic (rate dependent) media including residual stresses.

3.2.1. General remarks

The numerical implementation of the current model complies with the use of a thermo-mechanically coupled FE formulation. This scheme has been already exploited by different authors, see Ostwald and co-authors [82] for its application to nonlocal regularized damage models and Navidtehrani and co-authors. [83, 84] for phase field methods. In particular, we exploit a modified version of the numerical approach developed in [83] in the software ABAQUS using a user material subroutine UMAT in conjunction to the functionality HETVAL, that provides an internal heat generation in heat transfer analysis at the integration point level[1]. The principal reason motivating this option for the current numerical framework is twofold: (i) from the user's perspective, it is not required to implement a user-defined element via the subroutine UEL of ABAQUS for the phase field governing functional and, (ii) the use of the initial state dependent variable routine SDVINI for the incorporation of residual stresses can be employed without any restriction.

According to Navidtehrani and coauthors [83, 84], the resulting coupled thermo-mechanical problem is solved using a staggered iterative solution for the obtention of the solution of the displacement and the phase field variables. Note that staggered iterative solution procedures generally require the use of sufficiently small load increments in order to ensure that the solution does not deviate from the equilibrium one [34]. Concerning the FE mesh characteristics, the present formulation are integrated into first-order hexahedral (quadrangular in 2D) hybrid elements with full integration.

Regarding the mechanical sub-problem, the mechanical user-defined material model using the UMAT capability requires the computation of the Cauchy stress tensor (STRESS in ABAQUS), the mechanical tangent (DDSDDE in ABAQUS), and the state dependent variables vector STATEV. In line with the derivation presented in Sec. 2.2, the material formulation is formulated in terms of the right Cauchy-Green deformation tensor $\mathbf{C}$ and the second Piola-Kirchhoff stress tensor $\mathbf{S}$. The Cauchy stress tensor $\boldsymbol{\sigma}$ can be obtained from a weighted push-forward of $\mathbf{S}$ such that $\boldsymbol{\sigma} = J^{-1}\varphi_*[\mathbf{S}]$, see Eq. (35) for the corresponding definition. The mechanical tangent can be accordingly derived as is presented in Sec. 2.2. Finally, a set of state dependent variables is also defined encompassing: (i) the current value of the free-energy function, (ii) the maximum value of the driving force $\mathcal{H}$ throughout the loading process, (iii) the fracture toughness, and

---

[1]This is required since previous versions of ABAQUS 2019 do not compute properly the volumetric heat generation.

(iv) the length scale parameter.

With respect to the thermal problem, we start the derivation from the local spatial form of the heat equation. Assuming an homogeneous and temperature independent mass density ρ, a homogenous and temperature independent heat capacity c_p, and thermal isotropy recalling the Duhamel's law of heat conduction that yields to Fourier's law, $\mathbf{q} = -k\nabla_{\mathbf{x}}\vartheta$ (where $\mathbf{q}$ is the heat flux, thermal conductivity k and $\nabla_{\mathbf{x}}\vartheta$ is the gradient of the temperature ϑ), the heat equation can be expressed as:

$$\rho c_p \frac{\partial \vartheta}{\partial t} - k\nabla_{\mathbf{x}} \cdot [\nabla_{\mathbf{x}}\vartheta] = r_{\vartheta}, \tag{33}$$

where r_{ϑ} is the spatial heat source.

The governing equation, Eq.(32) for the phase field resembles the form of the heat equation given in Eq. (33) after rearranging some of the terms. The main difference between both expressions lies in the computation of the gradient of phase field variable that should be mapped onto the current configuration. For this purpose we recall standard push-forward operations, where the gradient of the phase field in analogy with the temperature:

$$\nabla_{\mathbf{x}}\mathfrak{d} = \mathbf{F}^{-\mathrm{T}}\nabla_{\mathbf{X}}\mathfrak{d} \tag{34}$$

Moreover, in line with Hortig [85], a unit mass density can be defined yielding to the identification of the variable χ with the heat capacity c_p, whereas the heat generation should be also activated and setting as material property the thermal conductivity k equal to 1.

3.2.2. Derivation of the numerical implementation of the constitutive model

To fully implement the `UMAT` subroutine, the stress field and the Jacobian matrix are required to be computed for the current system of coordinates. For that reason, there is a need to perform a push-forward operation for these magnitudes to obtain the Cauchy stress and the spatial constitutive tensor. It is important to highlight that all the calculations are made for the reference configuration and then, we push-forward the required variables at the end to adjust to the requirements of the `UMAT` subroutine.

Starting with the terms for the stresses, these are known to be easily computed by doing the following product to the different terms for the second Piola-Kirchhoff stress in Eq. (20)

$$\boldsymbol{\sigma} = J^{-1}\mathbf{F}\mathbf{S}\mathbf{F}^{\mathrm{T}}. \tag{35}$$

This operation is straightforward for the terms related to the hyperelastic (Eq. (8)) and the prestresses (Eq. (18)). However, it is important to highlight some remarks about the evolution in time of the viscous stresses (Eq. (13)), regarding the time dependence of the tensor $\mathbf{A}$, which needs to be properly addressed. This magnitude is updated for every iteration in the staggered scheme following the expression:

$$\mathbf{A}_{n+1}^{(\alpha)} = \mathbf{A}_n^{(\alpha)} + \Delta t \dot{\mathbf{A}}_{n+1}^{(\alpha)} \tag{36}$$

which can be developed by considering the expression for $\dot{\mathbf{A}}^{(\alpha)}$ in Eq. (11) as

$$\mathbf{A}_{n+1}^{(\alpha)} = \left(\frac{1}{1 + \Delta t/\tau^{(\alpha)}}\right)\left[\mathbf{A}_n^{(\alpha)} + \frac{\Delta t}{\tau^{(\alpha)}}(\bar{\mathbf{C}}_{n+1}^{-1})\right]. \tag{37}$$

Subsequently after this, we decide to perform the push-forward operation in the tensor $\mathbf{A}^{(\alpha)}$ like: $\mathbf{a}_{n+1}^{(\alpha)} = \mathbf{F}_{n+1}\mathbf{A}_{n+1}^{(\alpha)}\mathbf{F}_{n+1}^{\mathrm{T}}$. The reason on why performing this action here rather than when computing $\mathbf{S}_{n+1}^{(\mathrm{visco},\alpha)}$ relies on a considerable improvement in the convergence rate. Therefore, after doing some algebra, the expression for the Cauchy viscous overstress in the UMAT is found

$$\boldsymbol{\sigma}_{n+1}^{(\mathrm{visco},\alpha)} = J^{-5/3}\left(\frac{\mu^{\mathrm{visco},\alpha}}{1 + \Delta t/\tau^{(\alpha)}}\right)\left[\mathbf{a}_{n+1}^{(\alpha)} - \frac{1}{3}\mathrm{tr}\big(\mathbf{a}_{n+1}^{(\alpha)}\big)\mathbf{1}\right]. \tag{38}$$

Next, in order to compute the material Jacobian in the current configuration, it is considered two separate terms: at first, one for the material (hyper-viscoelastic law), which has the formula of

$$\mathbb{C}_{ijkl}^{\mathrm{mat}} = \frac{1}{2}J^{-1}\left(F_{lm}\frac{\partial(J\sigma_{ij})}{\partial F_{km}} + F_{km}\frac{\partial(J\sigma_{ij})}{\partial F_{lm}}\right) \tag{39}$$

where

$$\begin{aligned}
\frac{\partial(J\sigma_{ij})}{\partial F_{km}} &= \mu J^{-2/3}\left(\delta_{ik}F_{jm} + \delta_{jk}F_{im} - \frac{2}{3}\delta_{ij}F_{km} - \frac{2}{3}b_{ij}F_{mk}^{-1} + \frac{2}{9}(\mathrm{tr}\mathbf{b})\delta_{ij}F_{mk}^{-1}\right) \\
&\quad + \kappa\delta_{ij}F_{mk}^{-1} + \sum_\alpha\left\{J^{-2/3}\left(\frac{\mu^{\mathrm{visco},\alpha}}{1 + \Delta t/\tau^{(\alpha)}}\right)\left[-\frac{2}{3}F_{lk}^{-1}(\bar{\mathbf{F}}_{n+1}\mathbf{A}_n^{(\alpha)}\bar{\mathbf{F}}_{n+1}^{\mathrm{T}})_{ij}\right.\right. \\
&\quad + \frac{2}{9}F_{lk}^{-1}\mathrm{tr}(\bar{\mathbf{F}}_{n+1}\mathbf{A}_n^{(\alpha)}\bar{\mathbf{F}}_{n+1}^{\mathrm{T}})\delta_{ij} + \delta_{ik}(\mathbf{A}_n^{(\alpha)}\bar{\mathbf{F}}_{n+1}^{\mathrm{T}})_{\mathrm{lj}} + (\bar{\mathbf{F}}_{n+1}\mathbf{A}_n^{(\alpha)})_{il}\delta_{jk} \\
&\quad \left.\left.- \frac{1}{3}(\mathbf{A}_n^{(\alpha)}\bar{\mathbf{F}}_{n+1}^{\mathrm{T}})_{lk}\delta_{ij} - \frac{1}{3}(\bar{\mathbf{F}}_{n+1}\mathbf{A}_n^{(\alpha)})_{kl}\delta_{ij}\right]\right\}.
\end{aligned} \tag{40}$$

On the other hand, the other Jacobian term accounts for the residual stresses contribution. Its stiffness matrix can be computed as

$$\mathbb{C}_{ijkl}^{\mathrm{res}} = \mathbb{C}_{ijkl}^{\mathrm{c,res}} + \frac{1}{2}(\delta_{ik}\sigma_{lj}^{\mathrm{res}} + \delta_{il}\sigma_{kj}^{\mathrm{res}} + \delta_{jl}\sigma_{ik}^{\mathrm{res}} + \delta_{jk}\sigma_{il}^{\mathrm{res}}), \tag{41}$$

$$\mathbb{C}_{ijkl}^{\mathrm{c,res}} = \frac{4}{J}F_{i\alpha}F_{j\beta}F_{k\gamma}F_{l\delta}\frac{\partial^2\Psi^{\mathrm{res}}}{\partial\mathbf{C}^2}\bigg|_{\alpha\beta\gamma\delta}. \tag{42}$$

For the second derivative, the following terms are needed

Table 1. Mechanical properties of the double-notched plane strain specimen.

Property (Unit)	μ (MPa)	κ (MPa)	μ^{visco} (MPa)	$\mathcal{G}_C$ (N/mm)	ℓ (mm)	f	χ
Value	0.41	3.96	0.36	20.0	2.0	0.5	10^{-16}

$$\frac{\partial \mathbf{C}^{-1}}{\partial \mathbf{C}}\bigg|_{ijkl} = \frac{1}{2}(C_{ik}^{-1}C_{lj}^{-1} + C_{il}^{-1}C_{kj}^{-1}), \tag{43}$$

$$\frac{\partial^2 I_6}{\partial \mathbf{C}^2}\bigg|_{ijkl} = \frac{1}{2}(\delta_{ik}\sigma_{0lj} + \delta_{il}\sigma_{0kj} + \delta_{jl}\sigma_{0ik} + \delta_{jk}\sigma_{0il}). \tag{44}$$

By employing them, one reaches

$$\frac{\partial^2 \Psi^{\text{res}}}{\partial \mathbf{C}^2}\bigg|_{\alpha\beta\gamma\delta} = J^{-1/3}\left[-\frac{f}{6}(\boldsymbol{\sigma_0} \otimes \mathbf{C}^{-1} + \mathbf{C}^{-1} \otimes \boldsymbol{\sigma_0}) + \frac{fI_5}{18}\mathbf{C}^{-1} \otimes \mathbf{C}^{-1} - \frac{fI_5}{6}\frac{\partial \mathbf{C}^{-1}}{\partial \mathbf{C}}\right]$$
$$+ (1-f)J^{-2/3}\left[\frac{I_6}{9}\mathbf{C}^{-1} \otimes \mathbf{C}^{-1} - \frac{1}{6}\left(\mathbf{C}^{-1} \otimes \frac{\partial I_6}{\partial \mathbf{C}} + \frac{\partial I_6}{\partial \mathbf{C}} \otimes \mathbf{C}^{-1}\right) - I_6\frac{\partial \mathbf{C}^{-1}}{\partial \mathbf{C}} + \frac{1}{4}\frac{\partial^2 I_6}{\partial \mathbf{C}^2}\right].$$

$$\tag{45}$$

Finally, both terms of Eqs. (39) and (41) are added to form the material Jacobian

$$\mathbb{C}_{ijkl} = \mathbb{C}_{ijkl}^{\text{mat}} + \mathbb{C}_{ijkl}^{\text{res}}. \tag{46}$$

4. Representative applications

4.1. Verification example

In order to verify the present hyperelastic and visco-hyperelastic formulation, a benchmark application is first considered. For this purpose, a two-dimensional plane strain example of a double-notched specimen conducted by Hocine and co-authors. [24] is taken as reference solution in conjunction with the corresponding correlation with experimental data. The geometric description is displayed in Fig. 4(a), whereas the material properties are listed in Tab. 1.

The topmost and bottommost edges of the specimen are subjected to a prescribed monotonic displacement along the Y-direction until complete failure. Current samples are discretized using two-dimensional 8000 first-order quadrangular elements of `ABAQUS`, considering only half of the domain due to symmetry conditions. Each simulation requires up to one hour of running time for one `16GB RAM` computing station with a `11th Gen Intel(R) Core(TM) i7-11800H` processor.
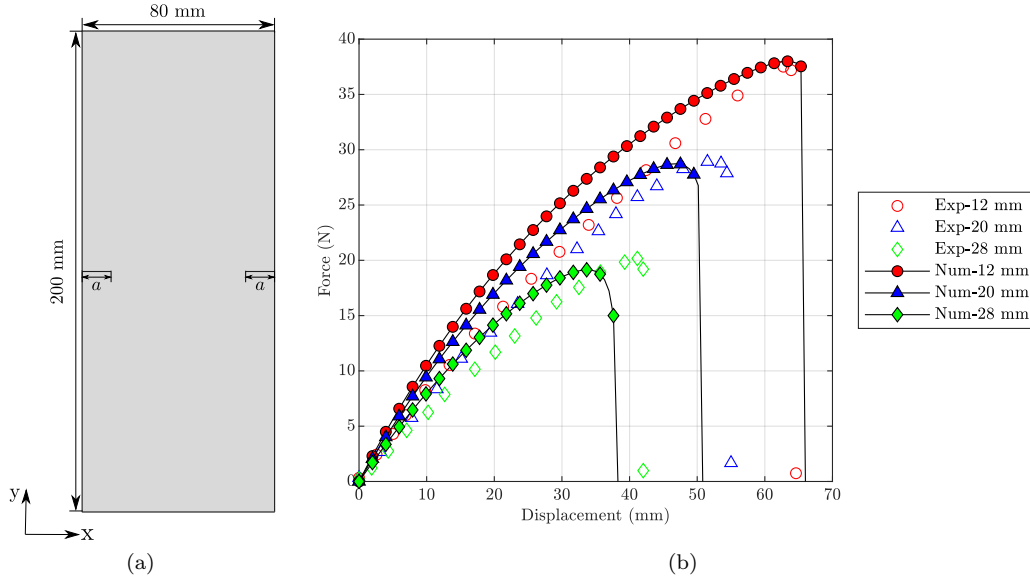
Figure 4. a) Geometry setup of the double-notched specimen conducted by [24] with b) the corresponding load-displacement curves (numerical, Num, and experimental, Exp) for verification , precluding viscous effects.

In line with previous phase field models [86, 87], the current formulation is first validated under rate-independent fracture evolution conditions. Fig. 4(b) shows the different load-displacement evolution curves for different sizes of the initial notches, exhibiting a very satisfactory correlation with respect to the available experimental tests for $a = [12, 20, 28]$ mm.

This application is further analyzed in order to elucidate the rate-dependent response, analyzing the effect of a series of relaxation times $\tau = [0.05, 0.1]$ s and velocities v $= [125, 250, 500, 1000]$ mm/s for a length of the prescribed notch $a = 20$ mm considering only one viscous sub-domain. The corresponding force-displacement evolution curves are depicted in Figs. 5(a)-5(b). Analyzing this graph it is possible to observe that the maximum force increases and the peak displacement decreases as the loading rate augments (both reported in Tab. 2).

Examining the mechanical response with respect to the relaxation time, the behaviour of a specimen at a constant loading rate v $= 500$ mm/s is compared in Fig. 6 for relaxation times $\tau = [0.01, 0.05, 0.1, 0.5]$ s. This graph evidences that smaller values of the relaxation times leads to higher values for the maximum displacement and smaller lower forces (see Tab. 3 for the values of these magnitudes). This response shows a very good qualitative correlation with the findings reported in [64]. The phase field evolution for one representative case is plotted in Fig. 7, where, as it is expected, the initiation and evolution of the crack complies with Mode I fracture.

A further verification of this case is reported in Appendix A, where this parametric study is repeated for a square single-notched plate and the outlined results display a similar behavior to the ones aforementioned in this Section.
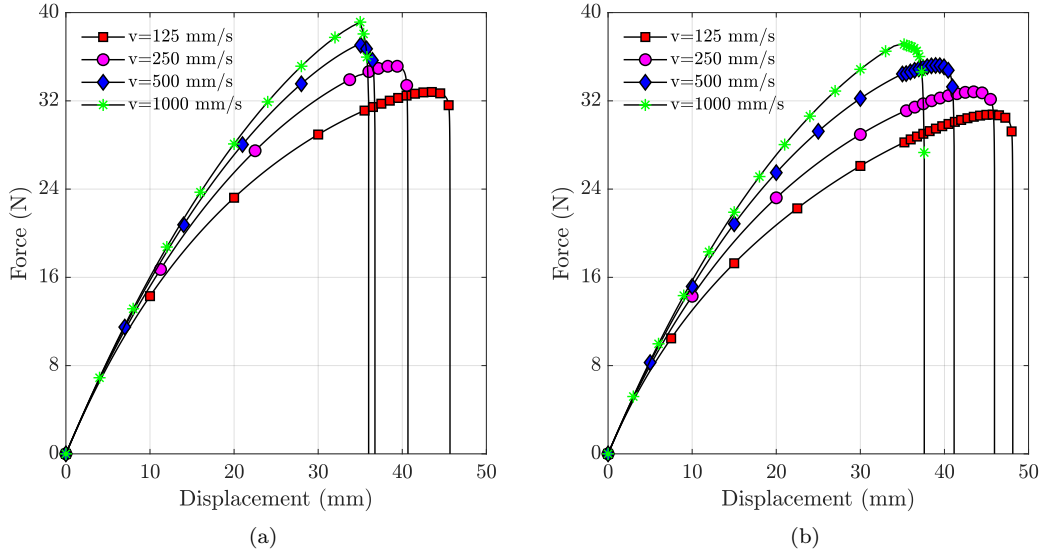
15

Figure 5. Load-displacement curves for tests with (a) $\tau = 0.1$ s and (b) $\tau = 0.05$ s and different displacement rates on the double-notched specimens.

Table 2. Comparison of the maximum force and displacement for different test rates on the double-notched specimen.

Displacement rate (mm/s)	1000	500	250	125
Relax time (s)	0.05 \ 0.1	0.05 \ 0.1	0.05 \ 0.1	0.05 \ 0.1
Maximum Force (N)	18.60 \ 19.57	17.60 \ 18.52	16.41 \ 17.58	15.38 \ 16.40
Maximum Displacement (mm)	37.60 \ 36.00	41.15 \ 36.75	45.95 \ 40.68	48.12 \ 45.68

4.2. Cylindrical structures

The main objective of this section concerns the simulation of pre-stressed cylindrical structures using the current modelling framework. For this purpose, a parametric analysis for hollow cylinders is conducted. Particularly, this is performed by modifying the viscous and residual intensity parameters in order to assess their influence on the mechanical performance of the structure.

The general features of the tests are presented in Sec. 4.2.1, which are used for the simulation of two baseline configurations: (i) intact hollow cylindrical structures (Sec. 4.2.2), and (ii) samples with a initial notch at the centre of the major axis (Sec. 4.2.3). It is worth mentioning that this initial notch is inserted via setting a prescribed boundary condition on the phase field value $\mathfrak{d} = 0.5$.

4.2.1. Test characteristics

This section describes the specimen geometry and the particular form of the residual stress field henceforth considered. In conjunction with the constitutive models for the bulk described above, we adopt the following form for the residual stress field, adapted
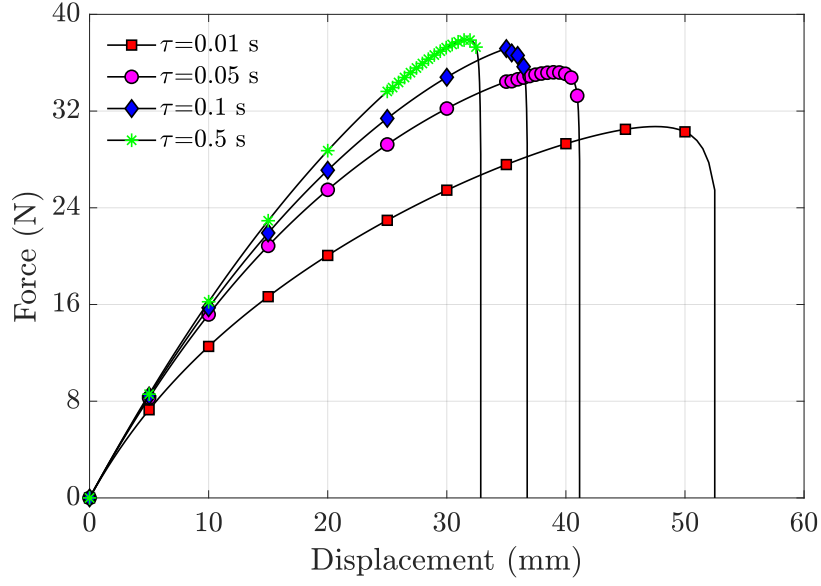
Figure 6. Load-displacement curves for tests with $v = 500$ mm/s and different relaxation times on the double-notched plane strain specimens.

Table 3. Comparison of the maximum force and displacement for different relaxation times of the double-notched specimen.

Displacement rate (mm/s)	500	500	500	500
Relax time(s)	0.01	0.05	0.1	0.5
Maximum Force (N)	18.95	18.58	17.60	15.36
Maximum Displacement (mm)	52.50	41.15	36.75	32.85

from [73, 88]:

$$\sigma_{0RR} = \alpha_c(R - A)(R - B) \tag{47}$$

$$\sigma_{0RZ} = \frac{\alpha_d}{R}[(R - A)(R - B)(4Z^3 - 6Z^2L + 2ZL^2)] \tag{48}$$

$$\sigma_{0\Theta\Theta} = \alpha_c[3R^2 - 2(A + B)R + AB] + \alpha_d[(R - A)(R - B)(12Z^2 - 12ZL + 2L^2)] \tag{49}$$

$$\sigma_{0ZZ} = -\frac{\alpha_d}{R}[(2R - A - B)(Z(L - Z))^2] \tag{50}$$

$$\sigma_{0\Theta Z} = \sigma_{0R\Theta} = 0 \tag{51}$$

where A and B are the inner and outer radius, respectively, of the cylindrical structure;

17
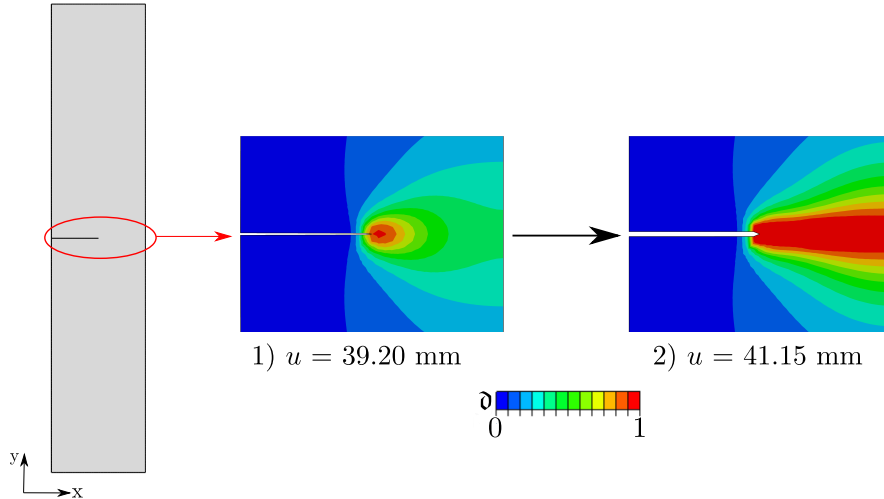
Figure 7. Zoom in the notched area during: Mode I (1) crack initiation and (2) propagation for the case with parameters v = 500mm/s and $\tau = 0.1$ s. Plotted is the phase field parameter isocontourn with the legend case, where blue and red denote intact and broken states, respectively.

Table 4. Mechanical properties of the cylindrical structures.

Property (Unit)	μ (MPa)	κ (MPa)	μ^{visco} (MPa)	$\mathcal{G}_{\text{C}}$ (N/mm)	ℓ (mm)	f	χ
Value	25.00	616.67	21.74	3.0	2.0	0	10^{-10}

α_c and α_d are coefficients which follow the formula $\alpha_c = \mu\bar{\alpha}_c/2BT$ and $\alpha_d = \mu\bar{\alpha}_d/2L^4$; and T and L are the thickness and length of the cylinder.

The strength of the residual stress field is controlled by the dimensionless parameters $\bar{\alpha}_c$ and $\bar{\alpha}_d$ which account for the dependence of the system on the R and Z coordinates of the cylindrical system. It follows that by setting $\bar{\alpha}_d = 0$, the pre-stress field only relies on R. Further research on how to obtain a qualitative behavior of the residual stress field for their different components can be found in [88].

Without any loss of generality, we prescribe the following dimensions for the cylinder: length $L = 150$ mm, diameter $D = 5$ mm and thickness $T = 0.5$ mm. Several simulations for the parametric tests are conducted by changing the displacement rate, relaxation time and the residual stresses field on cylinders with or without a phase field initial condition on the center for $\mathfrak{d} = 0.5$.

The mechanical properties for the current applications are listed in Tab. 4. Note that a nearly incompressible neo-Hookean material (ν=0.49) is set. Concerning the spatial discretization of the system, we employ 23250 8-node hexahedral elements with one viscous subdomain in the bulk material description.

In line with [69], present computations consist of two steps: (i) the first step is defined for the application of the residual stresses field presented in Eqs. (47)-(51), without prescribing any additional action, and (ii) the second step comprises the application of a pulling action along the longitudinal axis of the cylinder till the complete failure of the structure. Every numerical experiment requires one or two hours of computational run in the aforementioned station until its completion.

The BCs configuration for the geometry is like it follows: for the first step, the cylinder is restricted completely in the azimuthal direction in both topmost and bottommost
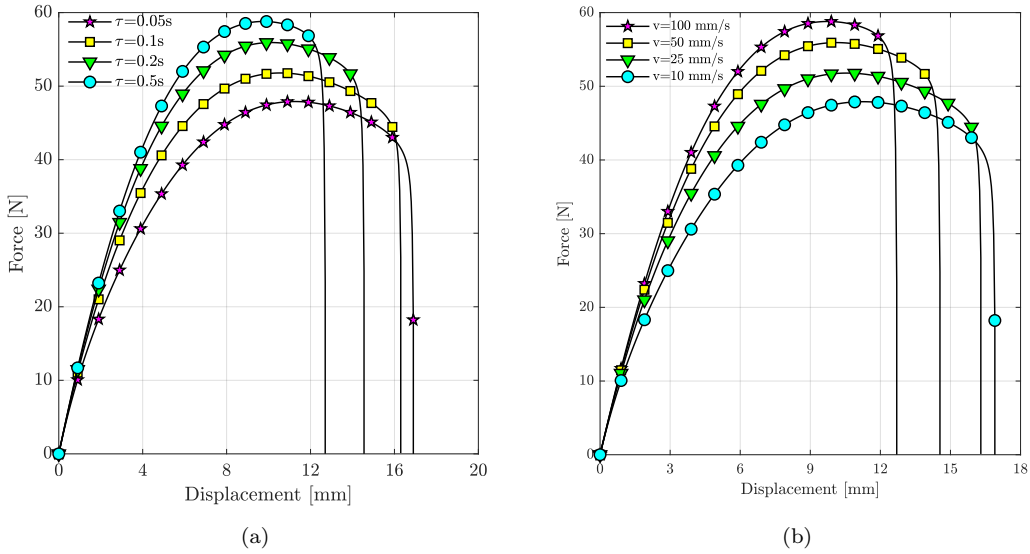
Figure 8. Load-displacement curves for cases with different (a) relaxation times and (b) displacement velocities for the non pre-stressed cylinders.

Table 5. Comparison of the maximum force and displacement for the tests with different relaxation times and v = 25 mm/s for the non pre-stressed cylinders.

Relax time (s)	0.05	0.1	0.2	0.5
Maximum Force (N)	48.60	51.79	55.93	59.16
Maximum Displacement (mm)	16.90	16.30	14.55	12.25

surfaces along the major axis in order to let the radial coordinate free for the application of the residual stresses. For the final step, the bottommost surface is fixed whereas the topmost surface is pulled in the Z direction until the failure of the cylindrical specimen.

4.2.2. Pristine cylinders

4.2.2.1. Dependence on visco-elastic parameters. The first series of parametric tests concerns the analysis of rate-dependent effects on crack propagation, in line with Sec. 4.1. Without the application of residual stress, the effect of different relaxation times $\tau = [0.05, 0.1, 0.2, 0.5]$ s and displacement rates v = $[10, 25, 500, 100]$ mm/s on the mechanical response of the current hollow cylinders are examined.

Results for the reaction force-imposed displacement evolution curves of the probes for different relaxation times and imposed velocities are obtained. Fig. 8(a) shows these curves for the different relaxation times setting v = 25 mm/s, whereas Fig. 8(b) depicts the results for $\tau = 0.1$ s and various displacement rates. Analyzing these plots, it can be seen that the dependence of the results on these viscoelastic parameters is in line with the verification results reported in Sec. 4.1, i.e. for higher relaxation time or test velocity the estimated peak force increases but ultimate displacement decreases. This trend is identified for all the cases under consideration as it is reported in Tabs.

19

Table 6. Comparison of the maximum force and displacement for the tests with different displacement rates and $\tau = 0.1$ s for the non pre-stressed cylinders.

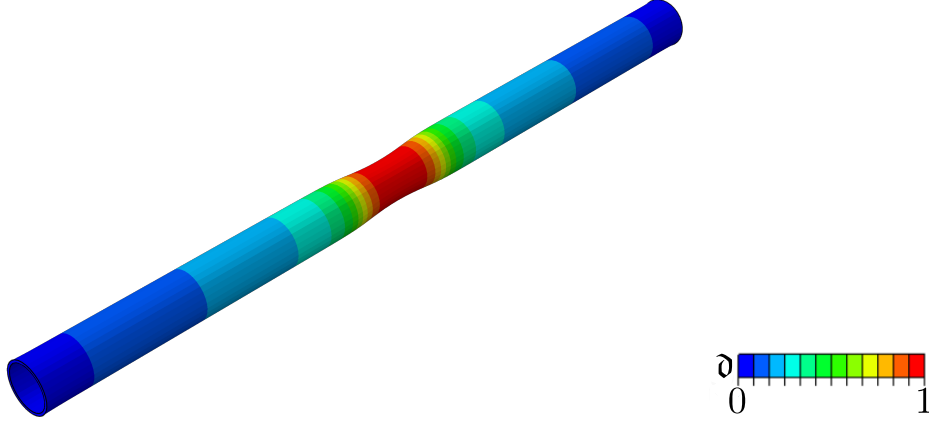| Displacement rate (mm/s)	100	50	25	10
Maximum Force (N)	58.80	55.93	51.79	47.91
Maximum Displacement (mm)	12.70	14.55	16.30	16.90

Figure 9. Phase field isocontour at the moment of failure for the non pre-stressed hollow cylinder.

5 and 6.

A representative phase field isocontour at the end of the computation is shown in Fig. 9 displaying that the crack initiates from the center of the probe and propagates axially provoking the failure of the specimen.

4.2.2.2. Dependence on residual stress parameters. Continuing with the numerical tests for pre-stressed pristine cylinders, the next two series of parametric computations are dedicated to the examination of the dependence of the results on both residual stress intensity factors $\bar{\alpha}_c$ and $\bar{\alpha}_d$. The effect of both parameters are analyzed separately in order to assess the damage that they cause to the cylindrical structures.

First, results for cases with plane residual stresses are considered ($\bar{\alpha}_c > 0$ and $\bar{\alpha}_d = 0$) with a prescribed velocity equal to v $= 25$ mm/s and a relaxation time of $\tau = 0.1$ s. Current predictions qualitatively coincide with that reported in [69] for the same residual stress field, whose von Mises stress isocontour at the step of the application of the residual stress is shown in Fig. 10. The reaction-force displacement curves for plane residual stress cases are depicted in Fig. 11. This graph reveals that both ultimate force and ultimate displacement decrease for greater values of the coefficient $\bar{\alpha}_c$. This can be concluded as expected since the inclusion of residual stresses is associated with a decrease in both strength and stiffness properties, which leads to premature failure.

For the sake of quantifying the curves, in Tab. 7, it is plotted both peak load and displacement for the overall experiment. It is worth highlighting that applications with higher residual stresses associated with $\bar{\alpha}_c > 3.5$ have been carried out but they are not considered since an abrupt change in the pattern of failure occurs, provoking in the model a severe radial strain.

Subsequently, specimens with both R- and Z-dependent residual stresses ($\bar{\alpha}_c = 0$
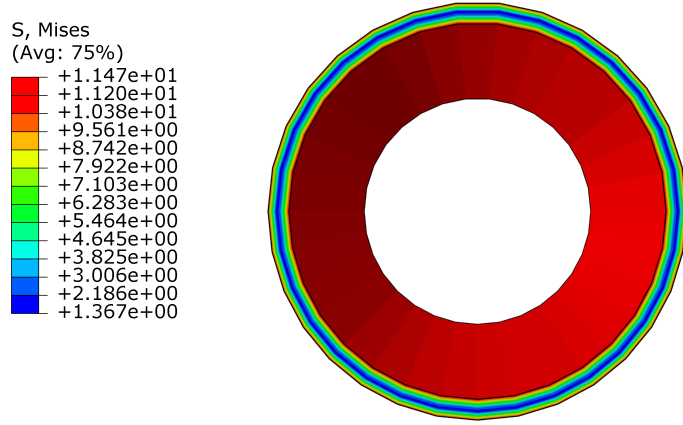
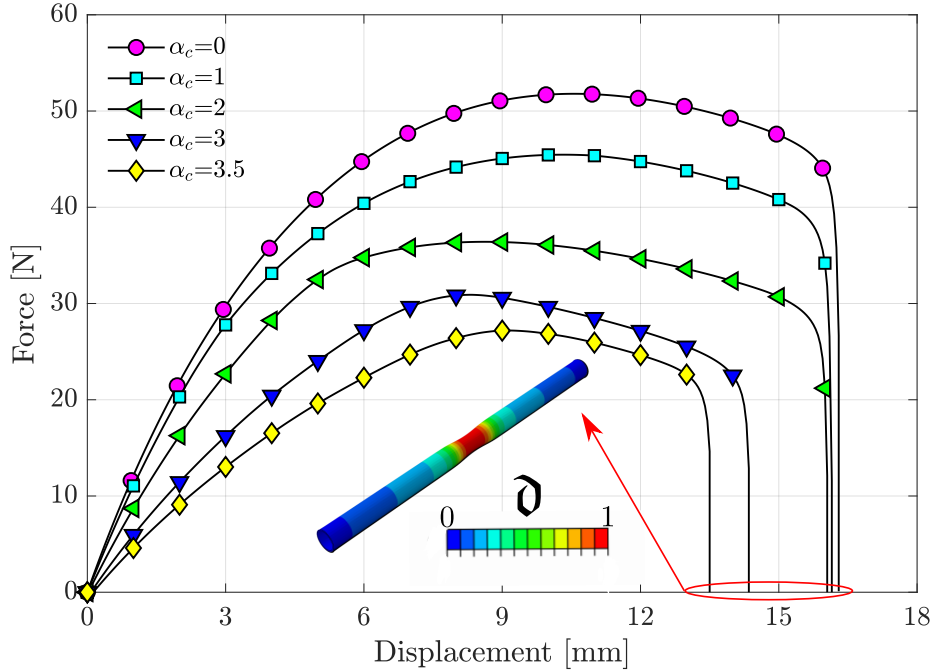**Figure 10.** Von Mises stresses distribution for a residual stress with $\bar{\alpha}_c = 1$.

Figure 11. Load-displacement curves for cylinders with different residual stress intensity parameter $\bar{\alpha}_c$, along with the phase field isocontour in the final step.

and $\bar{\alpha}_d > 0$) are taken into consideration in this last series of tests. Under these circumstances, a typical von Mises stresses isocontour is shown in Fig. 12 exhibiting an increase in the value of this magnitude (von Mises stress) while approaching the center of the major axis of the cylinder. This is in accordance with the patterns displayed in [88].

In line with the previous analysis for plane residual stresses, current load-displacement curves plotted in Fig. 13 show an overall similar trend, with some nuances: the higher the value of $\bar{\alpha}_d$ is set, the lower the values of the maximum force and maximum displacement are obtained, being considerably increased this difference for $\bar{\alpha}_d > 50$, when the peak values collapse due to this effect (see Tab. 8 for exact results).

Table 7. Comparison of the maximum force and ultimate displacement for the tests with different $\bar{\alpha}_c$.

$\bar{\alpha}_{\mathbf{c}}$	0	1	2	3	3.5
Maximum Force (N)	51.79	45.47	36.41	30.91	27.19
Maximum Displacement (mm)	16.30	16.15	16.05	14.35	13.50
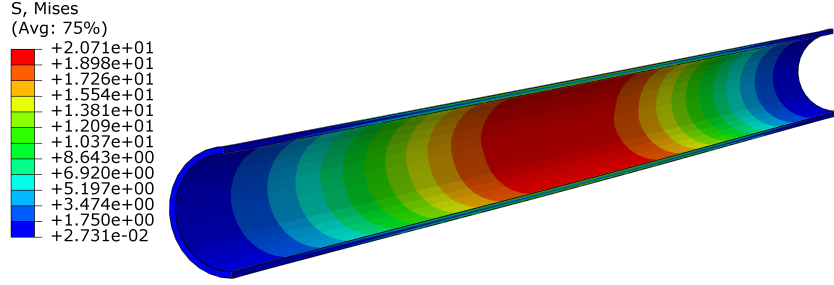
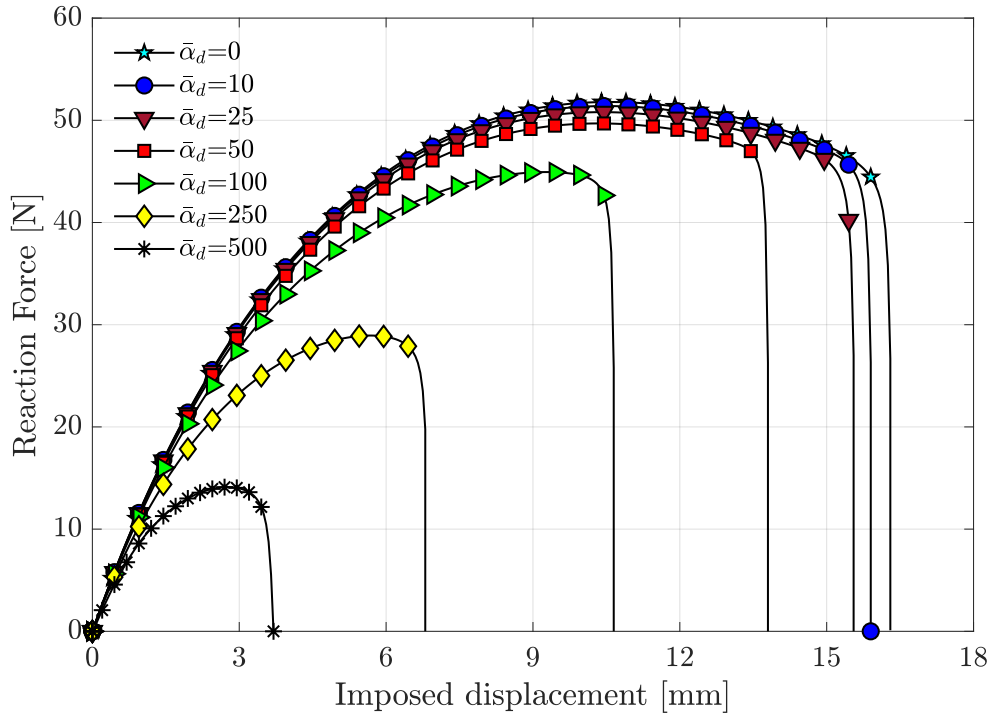**Figure 12.** Von Mises stresses distribution associated with a residual stress field in which $\bar{\alpha}_d = 500$.

Figure 13. Load-displacement curves for cylinders with different residual stress intensity parameters $\bar{\alpha}_d$.

In addition to this, it can be identified that the nucleation zone for failure is more concentrated towards the centre of the major axis for higher values of $\bar{\alpha}_d$, see Fig. 14.

22

Table 8. Comparison of the maximum force and ultimate displacement for the tests with different $\bar{\alpha}_d$.

$\bar{\alpha}_\mathbf{d}$	0	10	25	50	100	250	500
Maximum Force (N)	51.79	51.39	50.79	49.70	44.93	28.94	14.12
Maximum Displacement (mm)	16.30	15.90	15.55	13.80	10.65	6.80	3.70

(a) $\bar{\alpha}_d = 0$ (b) $\bar{\alpha}_d = 50$

(c) $\bar{\alpha}_d = 250$

$\mathfrak{d}$ ▮▮▮▮▮▮▮▮▮
0   1
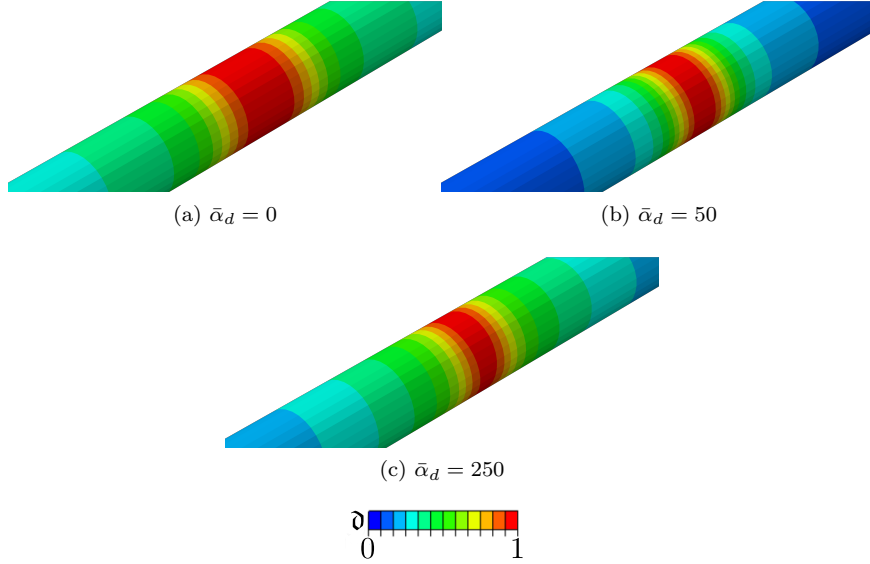
Figure 14. Phase field isocontour at the moment of failure for the residually stressed hollow cylinder with different values of $\bar{\alpha}_d$.

4.2.3. Cylinders with a initial flaw prescribing the phase field values at the center of the geometry

This section is focused on analyzing cases with a prescribed initial defect at the center of the cylinder. This is incorporated into the simulation by setting an initial value of the phase field variable at this location of $\mathfrak{d} = 0.5$. Current simulations are carried out with a displacement rate of v $=$ 25 mm/s and a relaxation time $\tau = 0.1$ s for a cylinder with the material parameters given in Tab. 1.

The corresponding reaction-force displacement curves for these cases are shown in Fig. 15. These results display that while the peak force is reduced slightly with the application of the phase field initial condition, the main difference between scenarios with and without prescribed initial defect concerns the premature failure of the structure, which is predicted to occur when initial flaw is considered, see Tab. 9.

Figs. 16(a) and 16(b) depict the initial state of the phase field variable and its propagation, respectively, in a representative case for a hollow cylinder with an initial flaw.
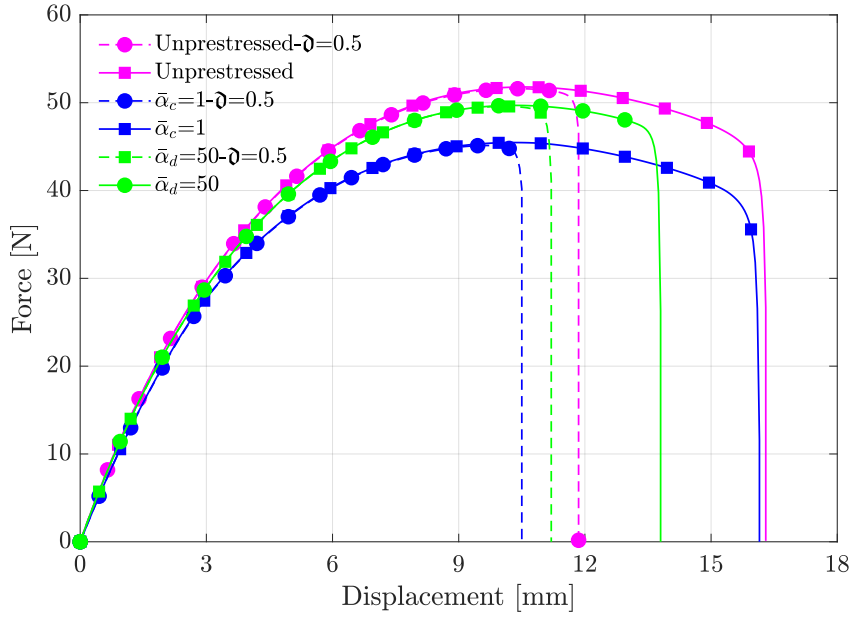
Figure 15. Load-displacement curves comparing the tests on cylinders with no residual stress, with $\bar{\alpha}_c = 1$ and $\bar{\alpha}_d = 40$ and additional cases with $\mathfrak{d} = 0.5$ as it is indicated in the labels of the curves.

Table 9. Comparison of the maximum force and ultimate displacement obtained in the tests with and without flaw for both pre-stressed and non pre-stressed cylinders.

Residual stresses	No		$\bar{\alpha}_\mathbf{c} = 1$		$\bar{\alpha}_\mathbf{d} = 50$	
$\mathfrak{d}$ BC	$\mathfrak{d} = 0.5$	$\mathfrak{d} = 0$	$\mathfrak{d} = 0.5$	$\mathfrak{d} = 0$	$\mathfrak{d} = 0.5$	$\mathfrak{d} = 0$
Maximum Force (N)	51.59	51.79	45.14	45.46	49.58	49.70
Maximum displacement (mm)	11.85	16.30	10.50	16.15	11.20	13.80

(a)   (b)

$\mathfrak{d}$ 0   1
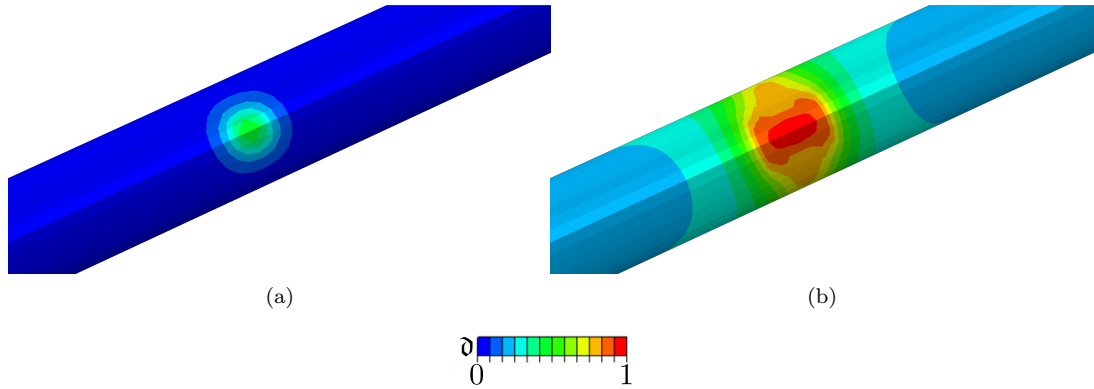
Figure 16. Axial propagation of the phase field parameter for the cylinders with the BC of $\mathfrak{d} = 0.5$: (a) first step and (b) last load step (axial propagation).
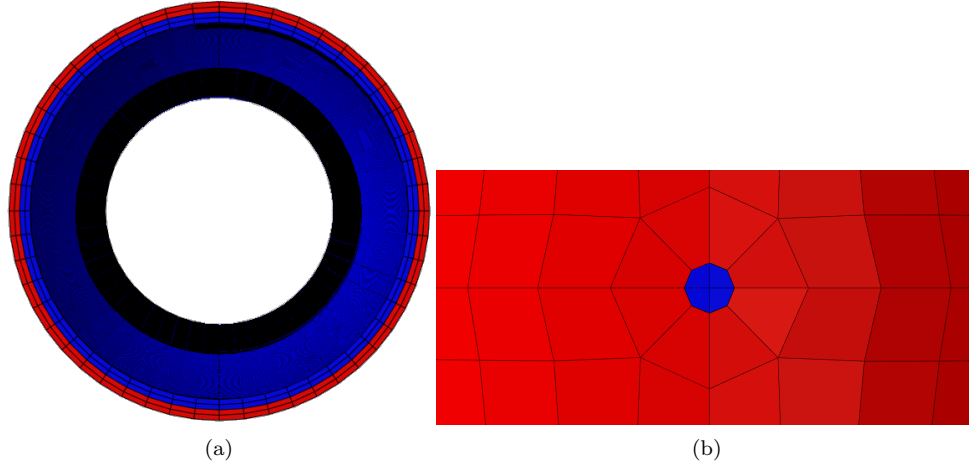
Figure 17. (a) Isommetric and (b) zoomed-in-the-notch view of the cylindrical structure with two layers, distinguishing the layer by the color.

4.3. Two-layered cylinders

4.3.1. Test characteristics

The simulation capabilities of the proposed model are further examined by considering multilayered cylindrical structures. The two-layered cylinder systems are particularized as follows: (i) a prescribed flaw over the thickness with a radius of 0.1 mm is defined at the center of the outer layer, and (ii) a residual stress field with $\bar{\alpha}_c = 0.5$ and $\bar{\alpha}_d = 40$ is set at the inner layer of the system, see the details displayed in Figs. 17(a)-17(b). The goal is to show that the methodology at hand can be used to handle these structures. A residual stress field is established in the inner layer of the cylinder, which

triggers a residual stress field in the outer layer, as, in general, displacements and radial components of traction have to be continuous through the interface. Numerically, some iterations might be needed to establish the initial equilibrium of the residually-stressed tube.

For the particularization of the system, a nearly incompressible neo-Hookean material is employed (ν =0.49) using a finite element mesh of 50024 8-node hexahedral elements. Each test requires a run time in the aforementioned station between 1-2 hours for its the completion.

The test conditions are as follows: a displacement rate of v $=$ 25 mm/s and a relaxation time $\tau = 0.1$ s for only one viscous subdomain are employed. The BCs do coincide with those presented in Sec. 4.2, with the exception that now in the step for the application of the residual stresses, only the inner bottommost and topmost surfaces are restricted in the azimuthal direction.

A parametric study is conducted to analyze the influence of the mismatch in several mechanical parameters on the behaviour of the sample, in particular, on the crack initiation region and on the mechanical performance of the sample. Special attention is paid to the effect of: (i) different shear modulus ratios (Sec. 4.3.2) and (ii) different critical fracture energy ratios (Sec. 4.3.3).

For the current parametric analysis, the inner region is kept unchanged in terms of some mechanical properties with respect to previous analyses, and those values are listed in Tab. 10. The only parameter that takes different values (compared to the

25

Table 10. Mechanical properties of the inner cylindrical layer.

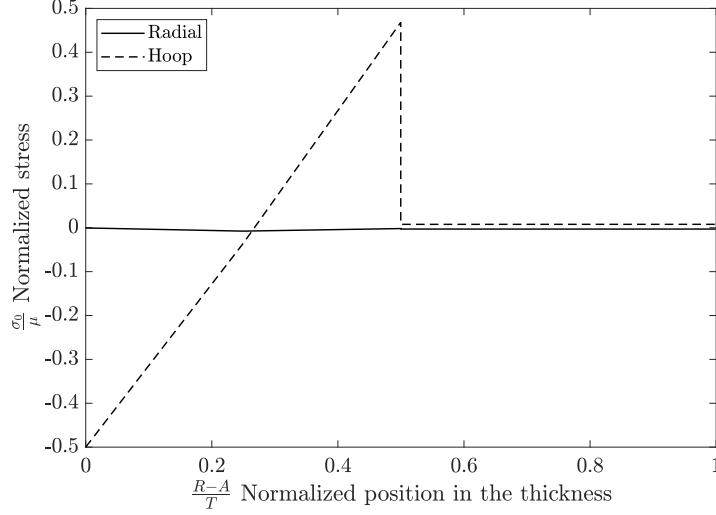| Property (Unit)	μ (MPa)	κ (MPa)	μ^{visco} (MPa)	G_C (N/mm)	ℓ (mm)	f	χ
Value	10	500	12	0.1	1.2	0	10^{-10}

Figure 18. Values of hoop and radial residual stresses along the thickness of the cylinder structure for a path located at Z = L/4.
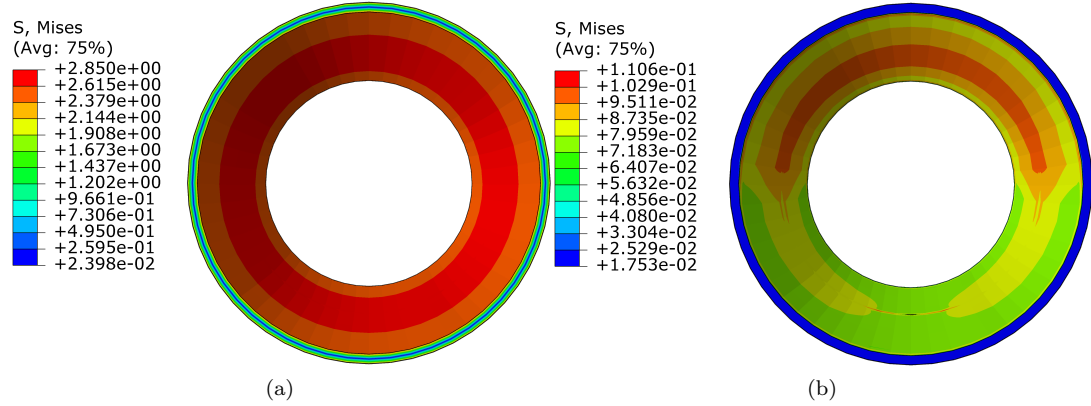

Figure 19. Von Mises stress isocontourn for (a) the inner and (b) the outer layer, respectively, for a pre-stressed bi-layered cylindrical structure.

previous cases) is the residual stress field since it is considered simultaneously that $\bar{\alpha}_c = 0.5$-$\bar{\alpha}_d = 40$ [88]. Hoop ($\sigma_{\theta\theta 0}$) and radial (σ_{RR0}) stresses are represented across the thickness of the cylinder at Z = L/4 in Fig. 18. Results for both stresses in the inner layer of the cylinder $\left(\frac{R-A}{T} \leq 0.5 \right)$ replicate qualitatively those obtained in Figure 10 of [69], and shows that the procedure captures the initial stress field. In the outer layer, it is observed the presence of residual stresses. To compliment this result, the von Mises stresses in the inner and outer layer are displayed in Figs. 19(a)-19(b), where
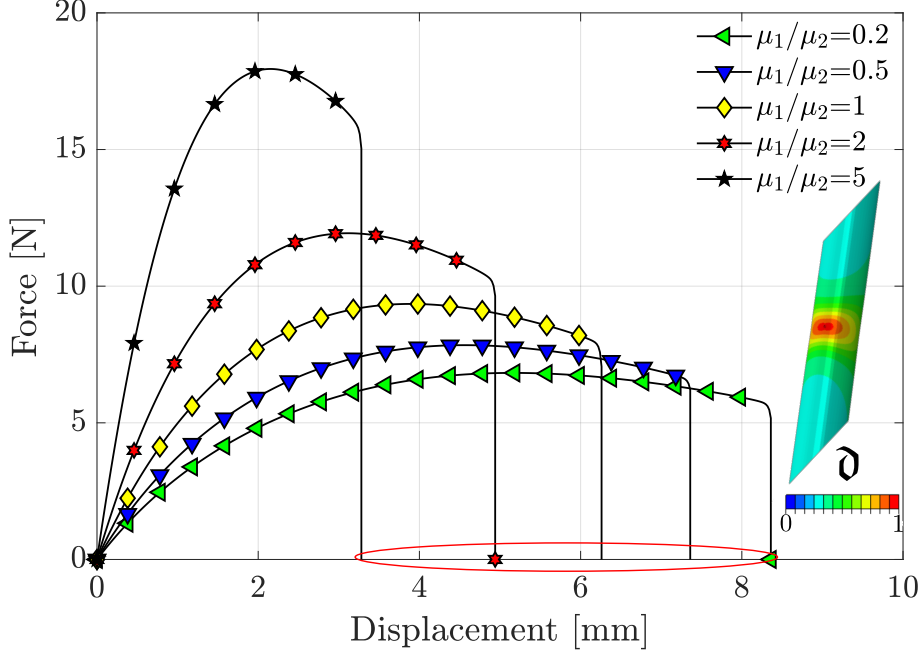
Figure 20. Reaction force-imposed displacement curves for the parametric study changing the shear modulus ratio without residual stress.

Table 11. Comparison of the maximum force and displacement for non pre-stressed two-layered cylinders with different μ_1/μ_2 ratios.

$\boldsymbol{\mu_1/\mu_2}$	0.2	0.5	1	2	5
Maximum Force (N)	6.83	7.84	9.35	11.94	17.95
Maximum Displacement (mm)	8.36	7.36	6.26	4.94	3.28

the difference in the magnitude of the stress field for both layers is pinpointed in the legend box of both isocontours.

4.3.2. Shear modulus influence

First, it is analyzed the role of the shear modulus ratio between both layers μ_1/μ_2, where the index 1 refers to the outer layer and the index 2 refers to the inner layer. The particular cases that are henceforth detailed concern the ratios: $\mu_1/\mu_2 = [0.2, 0.5, 1, 2, 5]$. Note that as the bulk modulus κ depends on μ and a fixed ratio of $\mu^{visc}/\mu = 1.2$ is considered, these parameters are also affected by the mismatch between μ_1 and μ_2.

Load-displacement curves for cases without residual stresses are depicted in Fig. 20. The failure displacement is increased for decreasing values of the ratio μ_1/μ_2 and, as it is expected, results feature a compliant response since the greater the ratio μ_1/μ_2 is, the greater is the mismatch between other corresponding mechanical properties ratios between the two layers. Failure reaction and imposed displacements are reported in Tab. 11 for several cases. From a qualitative point of view, the phase field isocontour at the final step is plotted, which displays a damage initiation region concentrated around the initial flaw for both outer and inner layers.
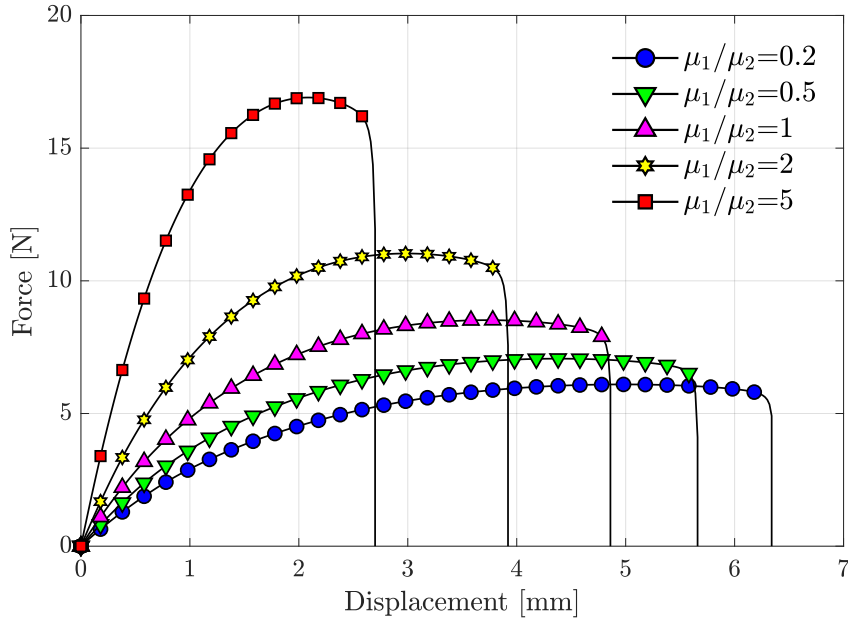
Figure 21. Reaction force-imposed displacement curves for the parametric study changing the shear modulus ratio with residual stress parameters $\bar{\alpha}_c = 0.5$-$\bar{\alpha}_d = 40$.

Table 12. Comparison of the maximum force and ultimate displacement for residually stressed ($\bar{\alpha}_c = 0.5 - \bar{\alpha}_d = 40$) two-layered cylinders with different μ_1/μ_2 ratios.

$\mathbf{\mu_1/\mu_2}$	0.2	0.5	1	2	5
Maximum Force (N)	6.10	7.07	8.52	11.03	16.91
Maximum Displacement (mm)	6.34	5.66	4.86	3.92	2.70

The residual stress field at the inner layer notably affects the response of the system. Force-displacement evolution curves are shown in Fig. 21, which exhibit the same behaviour as the non pre-stressed cases. Nevertheless, the effect of the residual stress can be appreciated in the specific failure magnitudes detailed in Tab. 12, where the values for both peak force and displacement are subtly smaller than the bi-layered cylinders without residual stress (see Tab. 11).

The effect of the shear modulus ratio on the pre-stressed cylinder is shown in Figs. 22(a)-22(e). From these graphs, it can be observed that the crack is captured to be initiated at the center, where the notch is located. Note also that the peak residual von Mises stress is at the center in the inner layer, see Fig. 19(a). Analyzing all the cases, one envisages that the μ ratio influences the crack initiation and propagation mode, displaying a dominant azimuthal pattern for $\mu_1/\mu_2 < 1$ (Figs. 22(a)-22(b)) which is switched to a Mixed-Mode propagating crack with both axial and circumferential modes for greater values of μ_1/μ_2 (Figs. 22(d)-22(e)).
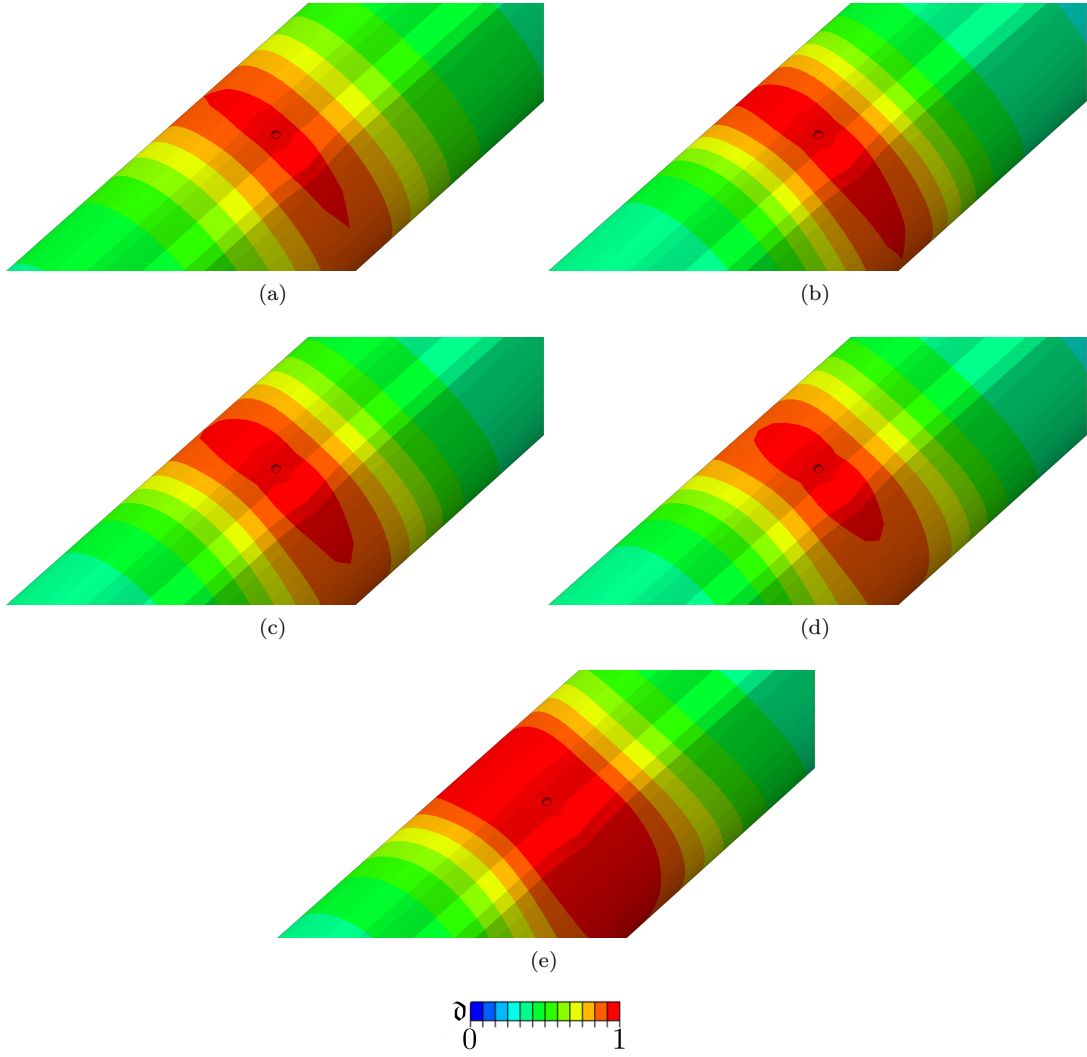
Figure 22. Crack pattern for the different critical Shear Modulus ratios with residual stress parameters $\bar{\alpha}_c = 0.5$-$\bar{\alpha}_d = 40$. Here displayed (a) $\mu_1/\mu_2 = 0.2$, (b) $\mu_1/\mu_2 = 0.5$, (c) $\mu_1/\mu_2 = 1$, (d) $\mu_1/\mu_2 = 2$ and (e) $\mu_1/\mu_2 = 5$.

4.3.3. Critical energy release rate influence

Considering now the role of $\mathcal{G}_C$, a mismatch of this parameter between both layers is studied, in particular, it is considered $\mathcal{G}_{C,1}/\mathcal{G}_{C,2} = [0.2, 0.5, 1, 2, 5]$. In the load-displacement curves depicted in Fig. 23 for cases without residual stresses, it is exhibited an expected behavior: when the $\mathcal{G}_C$ ratio (toughness) is increased the area under the curve grows i.e. the maximum load and displacement augment, being these values quantified in Tab. 13. Regarding a qualitative standpoint, by taking a look at the crack pattern, it is observed that nucleation is again located at the area (for both inner and outer layers) close to the notch, in agreement with the results for non pre-stressed probes from Sec. 4.3.2.

Taking into account residual stresses ($\bar{\alpha}_c = 0.5$ and $\bar{\alpha}_d = 40$), the load-displacement curves are plotted in Fig. 24. These curves follow the same behavior than the curves of Fig. 23 for non pre-stressed tubes, in the sense that peak force and displacement are
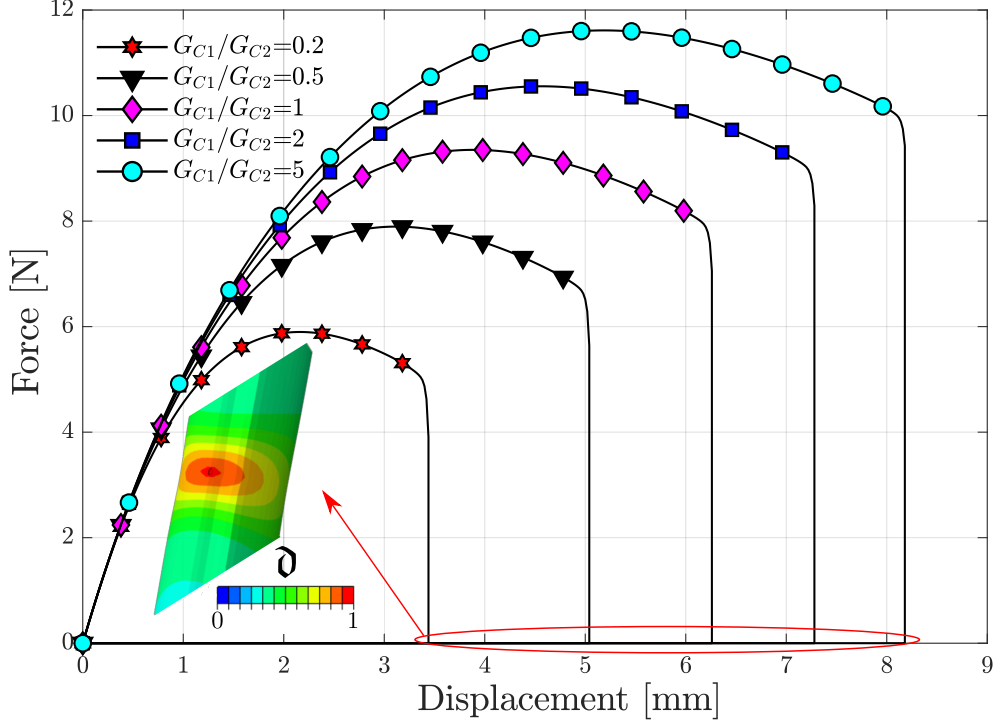
Figure 23. Reaction force-imposed displacement curves for the parametric study changing the critical energy release rate ratio without residual stress.

Table 13. Comparison of the maximum force and displacement for the tests with different $\mathcal{G}_C$ ratios in non pre-stressed two-layered cylinders.

$\mathcal{G}_{C,1}/\mathcal{G}_{C,2}$	0.2	0.5	1	2	5
Maximum Force (N)	5.90	7.90	9.35	10.55	11.61
Maximum Displacement (mm)	3.44	5.04	6.26	7.28	8.18

directly proportional to the ratio of critical strength (see Tab. 14). Nevertheless, the effect of the residual stresses is clearly observed in the crack pattern plotted for each case in Figs. 25(a)-25(e). The crack patterns display a fracture propagating azimuthally from the flawed region, being again consistent with the Von Mises stresses isocontourn displayed in Figs. 19(a)-19(b). The failure mechanism for different $\mathcal{G}_{C,1}/\mathcal{G}_{C,2}$ ratios is observed in the fracture initiation region, which shrinks for increasing values of the critical energy ratio.

5. Final remarks

Phase field methods for fracture simulation have evidenced several appealing aspects stemming from its inherent versatility to accommodate different mechanical behavior at the material point level. Exploiting a modular formalism, in this investigation, a novel phase field approach has been developed to simulate fracture events for residually stressed hyperelastic (rate independent) and visco-hyperelastic (rate dependent) hollow cylinders. The current computational model relies on the already proposed visco-
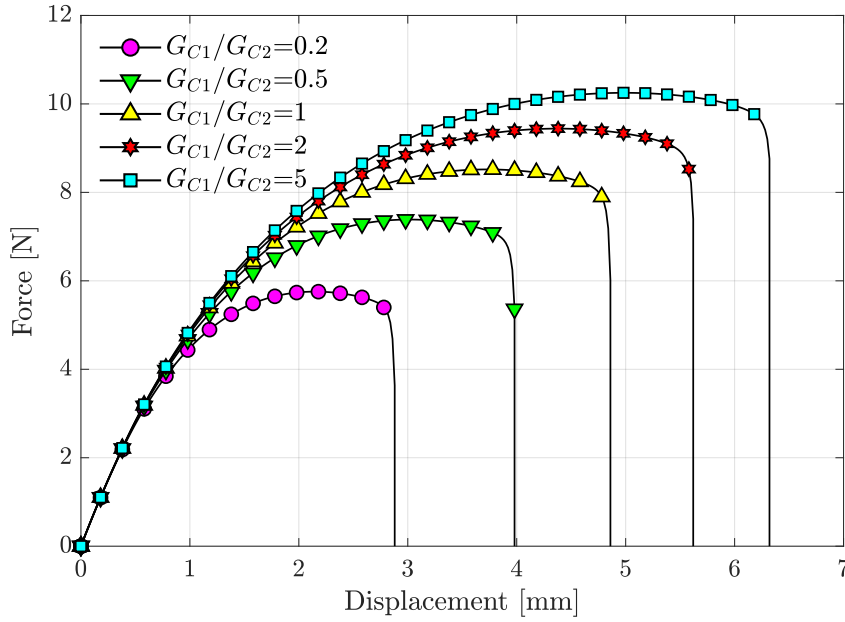
Figure 24. Reaction force-imposed displacement curves for the parametric study changing the critical energy release rate ratio with residual stress parameters $\bar{\alpha}_c = 0.5$-$\bar{\alpha}_d = 40$.

Table 14. Comparison of the maximum force and ultimate displacement for residually stressed ($\bar{\alpha}_c = 0.5 - \bar{\alpha}_d = 40$) two-layered cylinders with different $\mathcal{G}_C$ ratios.

$\mathcal{G}_{C1}/\mathcal{G}_{C2}$	0.2	0.5	1	2	5
Maximum Force (N)	5.76	7.39	8.52	9.44	10.25
Maximum Displacement (mm)	2.88	3.98	4.86	5.62	6.32

hyperelasticity theoretical formulation and it has been extended to consider residual stress fields in terms of an invariant-based formulation.

The proposed methodology was first validated against available experimental data featuring quasi-static fracture evolution. Subsequent parametric analysis examined the role of different mechanical aspects of the system in line with other works that use alternative phase field models for hyperelastic and visco-hyperelastic solids. Current simulations assessed the fracture of one-layered and two-layered cylindrical structures evaluating both viscous (τ and $\dot{u}$) and mechanical ($\mathcal{G}_C$ and μ mismatch) effects for several residual stress fields (which depend on the coordinates R and Z of the cylinder). Interestingly, the incorporation of residual stress fields in multi-layered cylindrical systems led to (a priori) unexpected results in terms of crack initiation and propagation mechanisms. This evidenced the need of the development of robust numerical frameworks that can take into consideration such effects.

Therefore, further extensions of this research would concern the application of this code to the analysis of bending and bulging instabilities in these kind of structures to simulate the fracture of arteries which suffer aneurysms, as well as the incorporation of anisotropic material laws in the layer-definition.
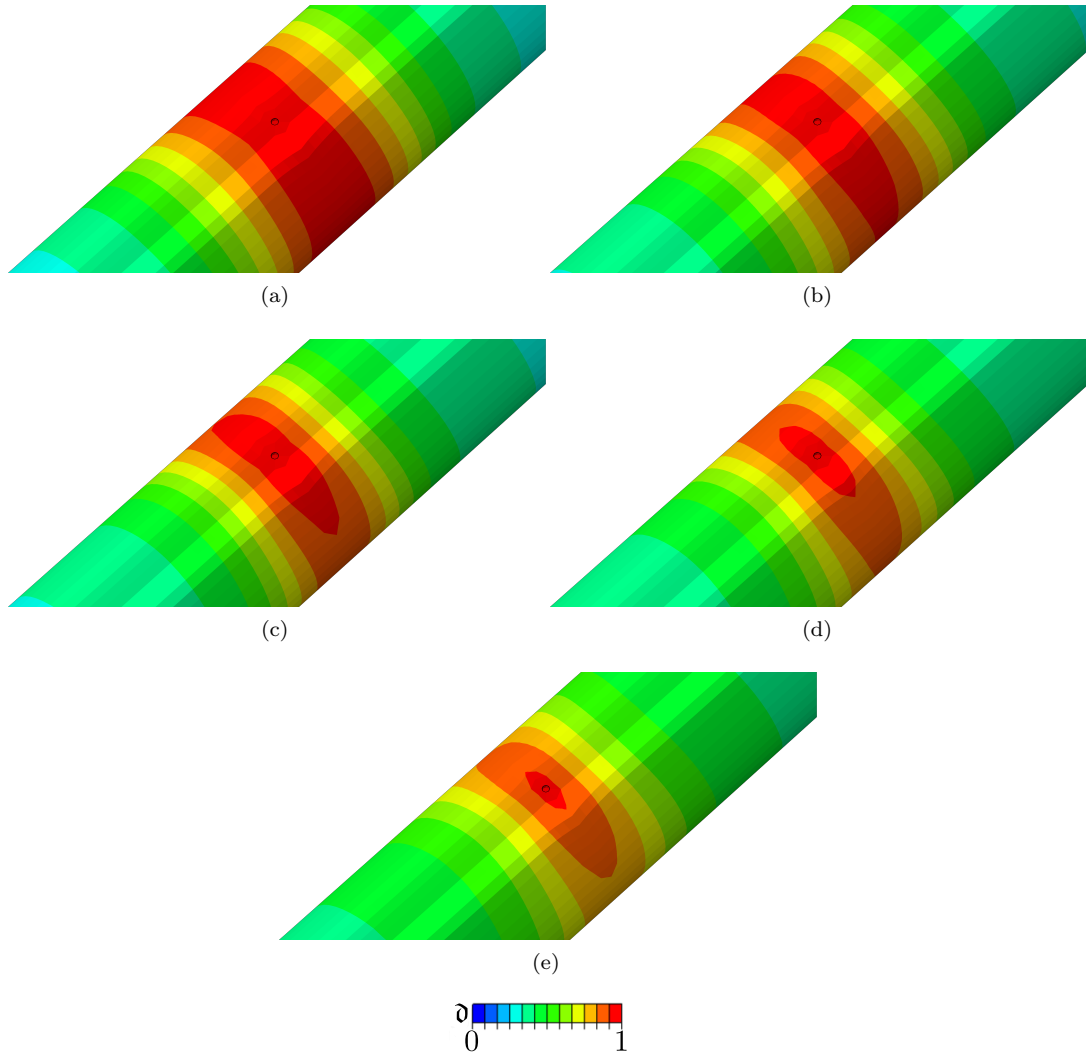
Figure 25. Crack pattern for the different critical energy release rate ratios with residual stress parameters $\bar{\alpha}_c = 0.5$-$\bar{\alpha}_d = 40$. Here displayed (a) $\mathcal{G}_{C1}/\mathcal{G}_{C2} = 0.2$, (b) $\mathcal{G}_{C1}/\mathcal{G}_{C2} = 0.5$, (c) $\mathcal{G}_{C1}/\mathcal{G}_{C2} = 1$, (d) $\mathcal{G}_{C1}/\mathcal{G}_{C2} = 2$ and (e) $\mathcal{G}_{C1}/\mathcal{G}_{C2} = 5$.

Declaration of competing interest

The authors declare that they have no known competing financial interests or personal relationships that could have appeared to influence the work reported in this paper.

Acknowledgements

References

[1] Y. Abou Msallem, F. Jacquemin, N. Boyard, A. Poitou, D. Delaunay, S. Chatel, Material characterization and residual stresses simulation during the manufacturing process of epoxy matrix composites, Composites Part A: Applied Science and Manufacturing 41 (1) (2010) 108–115, special Issue: Flow Processes in Composite Materials. doi:https://doi.org/10.1016/j.compositesa.2009.09.025.

[2] G. A. Holzapfel, R. W. Ogden, Modelling the layer-specific three-dimensional residual stresses in arteries, with an application to the human aorta, Journal of The Royal Society Interface 7 (46) (2010) 787–799. doi:https://doi.org/10.1098/rsif.2009.0357.

[3] N.-K. Jha, J. Reinoso, H. Dehghani, J. Merodio, A computational model for fiber-reinforced composites: hyperelastic constitutive formulation including residual stresses and damage, Computational Mechanics 63 (5) (2019) 931–948. doi:https://doi.org/10.1007/s00466-018-1630-5.

[4] J. D. Humphrey, Vascular adaptation and mechanical homeostasis at tissue, cellular, and sub-cellular levels, Cell Biochemistry and Biophysics 50 (2) (2008) 53–78. doi:https://doi.org/10.1007/s12013-007-9002-3.

[5] A. Alhayani, J. Giraldo, J. Rodríguez, J. Merodio, Computational modelling of bulging of inflated cylindrical shells applicable to aneurysm formation and propagation in arterial wall tissue, Finite Elements in Analysis and Design 73 (2013) 20–29. doi:https://doi.org/10.1016/j.finel.2013.05.001.

[6] A. Alhayani, J. Rodríguez, J. Merodio, Competition between radial expansion and axial propagation in bulging of inflated cylinders with application to aneurysms propagation in arterial wall tissue, International Journal of Engineering Science 85 (2014) 74–89. doi:https://doi.org/10.1016/j.ijengsci.2014.08.008.

[7] H. Demirkoparan, J. Merodio, Bulging bifurcation of inflated circular cylinders of doubly fiber-reinforced hyperelastic material under axial loading and swelling, Mathematics and Mechanics of Solids 22 (4) (2017) 666–682. doi:https://doi.org/10.1177/1081286515600045.

[8] J. Merodio, D. Haughton, Bifurcation of thick-walled cylindrical shells and the mechanical response of arterial tissue affected by marfan's syndrome, Mechanics Research Communications 37 (1) (2010) 1–6. doi:https://doi.org/10.1016/j.mechrescom.2009.10.006.

[9] N. Jha, J. Merodio, J. Reinoso, A general non-local constitutive relation for residually stressed solids, Mechanics Research Communications 101 (2019) 103421. doi:https://doi.org/10.1016/j.mechrescom.2019.103421.

[10] C. Linder, M. Tkachuk, C. Miehe, A micromechanically motivated diffusion-based transient network model and its incorporation into finite rubber viscoelasticity, Journal of the Mechanics and Physics of Solids 59 (10) (2011) 2134–2156. doi:https://doi.org/10.1016/j.jmps.2011.05.005.

[11] C. Miehe, J. Keck, Superimposed finite elastic–viscoelastic–plastoelastic stress response with damage in filled rubbery polymers. experiments, modelling and algorithmic implementation, Journal of the Mechanics and Physics of Solids 48 (2) (2000) 323–365. doi:https://doi.org/10.1016/S0022-5096(99)00017-4.

[12] J. Simo, On a fully three-dimensional finite-strain viscoelastic damage model: Formulation and computational aspects, Computer Methods in Applied Mechanics and Engineering

60 (2) (1987) 153–173. doi:https://doi.org/10.1016/0045-7825(87)90107-1.

[13] S. Govindjee, J. C. Simo, Mullins' effect and the strain amplitude dependence of the storage modulus, International Journal of Solids and Structures 29 (14) (1992) 1737–1751. doi:https://doi.org/10.1016/0020-7683(92)90167-R.

[14] G. A. HOLZAPFEL, On large strain viscoelasticity: Continuum formulation and finite element applications to elastomeric structures, International Journal for Numerical Methods in Engineering 39 (22) (1996) 3903–3926. doi:https://doi.org/10.1002/(SICI)1097-0207(19961130)39:22¡3903::AID-NME34¿3.0.CO;2-C.

[15] M. Kaliske, H. Rothert, Formulation and implementation of three-dimensional viscoelasticity at small and finite strains, Computational Mechanics 19 (3) (1997) 228–239. doi:https://doi.org/10.1007/s004660050171.

[16] N. Jha, J. Reinoso, H. Dehghani, J. Merodio, Constitutive modeling framework for residually stressed viscoelastic solids at finite strains, Mechanics Research Communications 95 (2019) 79–84. doi:https://doi.org/10.1016/j.mechrescom.2019.01.003.

[17] J. Bergström, M. Boyce, Constitutive modeling of the large strain time-dependent behavior of elastomers, Journal of the Mechanics and Physics of Solids 46 (5) (1998) 931–954. doi:https://doi.org/10.1016/S0022-5096(97)00075-6.

[18] S. Reese, S. Govindjee, A theory of finite viscoelasticity and numerical aspects, International Journal of Solids and Structures 35 (26) (1998) 3455–3482. doi:https://doi.org/10.1016/S0020-7683(97)00217-5.

[19] J. Merodio, K. R. Rajagopal, On constitutive equations for anisotropic nonlinearly viscoelastic solids, Mathematics and Mechanics of Solids 12 (2) (2007) 131–147. doi:https://doi.org/10.1177/1081286505055472.

[20] O. Lopez-Pamies, M. I. Idiart, T. Nakamura, Cavitation in elastomeric solids: I—a defect-growth theory, Journal of the Mechanics and Physics of Solids 59 (8) (2011) 1464–1487. doi:https://doi.org/10.1016/j.jmps.2011.04.015.

[21] W. G. Knauss, A review of fracture in viscoelastic materials, International Journal of Fracture 196 (1) (2015) 99–146. doi:https://doi.org/10.1007/s10704-015-0058-6.

[22] M. L. Cooke, D. D. Pollard, Fracture propagation paths under mixed mode loading within rectangular blocks of polymethyl methacrylate, Journal of Geophysical Research: Solid Earth 101 (B2) (1996) 3387–3400. doi:https://doi.org/10.1029/95JB02507.

[23] A. J. Pons, A. Karma, Helical crack-front instability in mixed-mode fracture, Nature 464 (7285) (2010) 85–89. doi:https://doi.org/10.1038/nature08862.

[24] N. A. Hocine, M. N. Abdelaziz, A. Imad, Fracture problems of rubbers: J-integral estimation based upon η factors and an investigation on the strain energy density distribution as a local criterion, International Journal of Fracture 117 (1) (2002) 1–23. doi:https://doi.org/10.1023/A:1020967429222.

[25] R. A. Schapery, Correspondence principles and a generalizedj integral for large deformation and fracture analysis of viscoelastic media, International Journal of Fracture 25 (3) (1984) 195–223. doi:https://doi.org/10.1007/BF01140837.

[26] M. Kroon, Steady-state crack growth in rubber-like solids, International Journal of Fracture 169 (1) (2011) 49–60. doi:https://doi.org/10.1007/s10704-010-9583-5.

[27] G. Geißler, M. Kaliske, M. Nase, W. Grellmann, Peel process simulation of sealed polymeric film computational modelling of experimental results, Engineering Computations 24 (6) (2007) 586–607. doi:https://doi.org/10.1108/02644400710774798.

[28] I. Zreid, R. Fleischhauer, M. Kaliske, A thermomechanically coupled viscoelastic cohesive zone model at large deformation, International Journal of Solids and Structures 50 (25) (2013) 4279–4291. doi:https://doi.org/10.1016/j.ijsolstr.2013.08.031.

[29] T. L. Warren, S. A. Silling, A. Askari, O. Weckner, M. A. Epton, J. Xu, A non-ordinary state-based peridynamic method to model solid material deformation and fracture, International Journal of Solids and Structures 46 (5) (2009) 1186–1195. doi:https://doi.org/10.1016/j.ijsolstr.2008.10.029.

[30] Y. Huang, S. Oterkus, H. Hou, E. Oterkus, Z. Wei, S. Zhang, Peridynamic model for visco-hyperelastic material deformation in different strain rates, Continuum Mechanics

and Thermodynamics (Nov 2019). doi:https://doi.org/10.1007/s00161-019-00849-0.

[31] A. Griffith, The Phenomena of Rupture and Flow in Solids, Philosophical Transactions A, 221 (1920) 163–198. doi:https://doi.org/10.1098/rsta.1921.0006.

[32] G. Francfort, J.-J. Marigo, Revisiting brittle fracture as an energy minimization problem, Journal of the Mechanics and Physics of Solids 46 (8) (1998) 1319–1342. doi:https://doi.org/10.1016/S0022-5096(98)00034-9.

[33] B. Bourdin, G. A. Francfort, J. J. Marigo, Numerical experiments in revisited brittle fracture, Journal of the Mechanics and Physics of Solids 48 (4) (2000) 797–826. doi:https://doi.org/10.1016/S0022-5096(99)00028-9.

[34] C. Miehe, F. Welshinger, M. Hofacker, Thermodynamically consistent phase-field models of fracture: Variational principles and multi-field FE implementations, International Journal for Numerical Methods in Engineering 83 (2010) 1273–1311. doi:https://doi.org/10.1002/nme.2861.

[35] C. Kuhn, R. Müller, A continuum phase field model for fracture, Engineering Fracture Mechanics 77 (18) (2010) 3625–3634. doi:https://doi.org/10.1016/j.engfracmech.2010.08.009.

[36] J.-Y. Wu, A unified phase-field theory for the mechanics of damage and quasi-brittle failure, Journal of the Mechanics and Physics of Solids 103 (2017) 72–99. doi:https://10.1016/j.jmps.2017.03.015.

[37] J.-Y. Wu, V. P. Nguyen, A length scale insensitive phase-field damage model for brittle fracture, Journal of the Mechanics and Physics of Solids 119 (2018) 20–42. doi:https://10.1016/j.jmps.2018.06.006.

[38] F. P. Duda, A. Ciarbonetti, P. J. Sánchez, A. E. Huespe, A phase-field/gradient damage model for brittle fracture in elastic-plastic solids, International Journal of Plasticity 65 (2015) 269–296. doi:https://doi.org/10.1016/j.ijplas.2014.09.005.

[39] C. Kuhn, T. Noll, R. Müller, On phase field modeling of ductile fracture, GAMM Mitteilungen 39 (1) (2016) 35–54. doi:https://doi.org/10.1002/gamm.201610003.

[40] M. J. Borden, T. J. R. Hughes, C. M. Landis, A. Anvari, I. J. Lee, A phase-field formulation for fracture in ductile materials: Finite deformation balance law derivation, plastic degradation, and stress triaxiality effects, Computer Methods in Applied Mechanics and Engineering 312 (2016) 130–166. doi:https://doi.org/10.1016/j.cma.2016.09.005.

[41] R. Alessi, M. Ambati, T. Gerasimov, S. Vidoli, L. De Lorenzis, Comparison of Phase-Field Models of Fracture Coupled with Plasticity, in: M. C. E. Oñate, D. Peric, E. de Souza-Neto (Ed.), Advances in Computational Plasticity, Springer International Publishing, Cham, 2018, pp. 1–21. doi:https://doi.org/10.1007/978-3-319-60885-3_1.

[42] A. Dean, J. Reinoso, N. Jha, E. Mahdi, R. Rolfes, A phase field approach for ductile fracture of short fibre reinforced composites, Theoretical and Applied Fracture Mechanics 106 (2020) 102495. doi:https://doi.org/10.1016/j.tafmec.2020.102495.

[43] B. Yin, M. Kaliske, A ductile phase-field model based on degrading the fracture toughness: Theory and implementation at small strain, Computer Methods in Applied Mechanics and Engineering 366 (2020) 113068. doi:https://doi.org/10.1016/j.cma.2020.113068.

[44] S. S. Shishvan, S. Assadpour-asl, E. Martínez-Pañeda, A mechanism-based gradient damage model for metallic fracture, Engineering Fracture Mechanics 255 (2021) 107927. doi:https://doi.org/10.1016/j.engfracmech.2021.107927.

[45] A. Raina, C. Miehe, A phase-field model for fracture in biological tissues, Biomechanics and Modeling in Mechanobiology 15 (3) (2016) 479–496. doi:https://doi.org/10.1007/s10237-015-0702-0.

[46] B. Li, C. Peco, D. Millán, I. Arias, M. Arroyo, Phase-field modeling and simulation of fracture in brittle materials with strongly anisotropic surface energy, International Journal for Numerical Methods in Engineering 102 (3-4) (2015) 711–727. doi:https://doi.org/10.1002/nme.4726.

[47] O. Gültekin, H. Dal, G. A. Holzapfel, A phase-field approach to model fracture of arterial walls: Theory and finite element analysis, Computer Methods in Applied Mechanics and Engineering 312 (2016) 542–566, phase Field Approaches to Fracture. doi:https://doi.org/10.1016/j.cma.2016.04.007.

[48] M. Paggi, M. Corrado, J. Reinoso, Fracture of solar-grade anisotropic polycrystalline silicon: A combined phase field–cohesive zone model approach, Computer Methods in Applied Mechanics and Engineering 330 (2018) 123 – 148. doi:https://doi.org/10.1016/j.cma.2017.10.021.

[49] O. Gültekin, H. Dal, G. A. Holzapfel, Numerical aspects of anisotropic failure in soft biological tissues favor energy-based criteria: A rate-dependent anisotropic crack phase-field model, Computer Methods in Applied Mechanics and Engineering 331 (2018) 23–52. doi:https://doi.org/10.1016/j.cma.2017.11.008.

[50] J. Storm, D. Supriatna, M. Kaliske, The concept of representative crack elements for phase-field fracture: Anisotropic elasticity and thermo-elasticity, International Journal for Numerical Methods in Engineering 121 (5) (2020) 779–805. doi:https://doi.org/10.1002/nme.6244.

[51] B. Yin, M. Kaliske, An anisotropic phase-field model based on the equivalent crack surface energy density at finite strain, Computer Methods in Applied Mechanics and Engineering 369 (2020) 113202. doi:https://doi.org/10.1016/j.cma.2020.113202.

[52] H. Ren, X. Zhuang, C. Anitescu, T. Rabczuk, An explicit phase field method for brittle dynamic fracture, Computers & Structures 217 (2019) 45–56. doi:https://doi.org/10.1016/j.compstruc.2019.03.005.

[53] C. Steinke, K. Özenç, G. Chinaryan, M. Kaliske, A comparative study of the r-adaptive material force approach and the phase-field method in dynamic fracture, International Journal of Fracture 201 (1) (2016) 97–118. doi:https://doi.org/10.1007/s10704-016-0125-7.

[54] P. K. Kristensen, E. Martínez-Pañeda, Phase field fracture modelling using quasi-Newton methods and a new adaptive step scheme, Theoretical and Applied Fracture Mechanics 107 (2020) 102446. doi:https://doi.org/10.1016/j.tafmec.2019.102446.

[55] M. Paggi, J. Reinoso, Revisiting the problem of a crack impinging on an interface:a modeling framework for the interaction between the phase field approach for brittle fracture and the interface cohesive zone model, Computer Methods in Applied Mechanics and Engineering 321 (2017) 145 – 172. doi:https://doi.org/10.1016/j.cma.2017.04.004.

[56] J. Reinoso, M. Paggi, C. Linder, Phase field modeling of brittle fracture for enhanced assumed strain shells at large deformations: formulation and finite element implementation, Computational Mechanics 59 (6) (2017) 981–1001. doi:https://doi.org/10.1007/s00466-017-1386-3.

[57] V. Carollo, J. Reinoso, M. Paggi, A 3D finite strain model for intralayer and interlayer crack simulation coupling the phase field approach and cohesive zone model, Composite Structures 182 (2017) 636–651. doi:https://doi.org/10.1016/j.compstruct.2017.08.095.

[58] V. Carollo, T. Guillén-Hernández, J. Reinoso, M. Paggi, Recent advancements on the phase field approach to brittle fracture for heterogeneous materials and structures, Advanced Modeling and Simulation in Engineering Sciences 5 (1) (2018) 8. doi:https://doi.org/10.1186/s40323-018-0102-y.

[59] T. Guillén-Hernández, I. G. García, J. Reinoso, M. Paggi, A micromechanical analysis of inter-fiber failure in long reinforced composites based on the phase field approach of fracture combined with the cohesive zone model, International Journal of Fracture 220 (2) (2019) 181–203. doi:https://doi.org/10.1007/s10704-019-00384-8.

[60] A. Quintanas-Corominas, J. Reinoso, E. Casoni, A. Turon, J. A. Mayugo, A phase field approach to simulate intralaminar and translaminar fracture in long fiber composite materials, Composite Structures 220 (2019) 899–911. doi:https://doi.org/10.1016/j.compstruct.2019.02.007.

[61] S. Goswami, C. Anitescu, S. Chakraborty, T. Rabczuk, Transfer learning enhanced physics informed neural network for phase-field modeling of fracture, Theoretical and Applied Fracture Mechanics 106 (2020) 102447. doi:https://doi.org/10.1016/j.tafmec.2019.102447.

[62] R. Shen, H. Waisman, L. Guo, Fracture of viscoelastic solids modeled with a modified phase field method, Computer Methods in Applied Mechanics and Engineering 346 (2019) 862–890. doi:https://doi.org/10.1016/j.cma.2018.09.018.

[63] P. J. Loew, B. Peters, L. A. Beex, Rate-dependent phase-field damage modeling of rubber and its experimental parameter identification, Journal of the Mechanics and Physics of Solids 127 (2019) 266–294. doi:https://doi.org/10.1016/j.jmps.2019.03.022.

[64] B. Yin, M. Kaliske, Fracture simulation of viscoelastic polymers by the phase-field method, Computational Mechanics 65 (2020) 293309. doi:https://doi.org/10.1007/s00466-019-01769-1.

[65] J. Song, L. Zhao, H. Qi, S. Li, D. Shi, J. Huang, Y. Su, K. Zhang, Coupling of phase field and viscoplasticity for modelling cyclic softening and crack growth under fatigue, European Journal of Mechanics - A/Solids 92 (2021) 104472. doi:https://doi.org/10.1016/j.euromechsol.2021.104472.

[66] F. Dammaß, M. Ambati, M. Kästner, A unified phase-field model of fracture in viscoelastic materials, Continuum Mechanics and Thermodynamics 33 (4) (2021) 1907–1929. doi:https://doi.org/10.1007/s00161-021-01013-3.

[67] P. Thamburaja, K. Sarah, A. Srinivasa, J. Reddy, Fracture of viscoelastic materials: Fem implementation of a non-local & rate form-based finite-deformation constitutive theory, Computer Methods in Applied Mechanics and Engineering 354 (2019) 871–903. doi:https://doi.org/10.1016/j.cma.2019.05.032.

[68] K. Sarah, P. Thamburaja, A. Srinivasa, J. N. Reddy, Numerical simulations of damage and fracture in viscoelastic solids using a nonlocal fracture criterion, Mechanics of Advanced Materials and Structures 27 (13) (2020) 1085–1097. doi:10.1080/15376494.2020.1716414.

[69] J. Rodríguez, J. Merodio, Helical buckling and postbuckling of pre-stressed cylindrical tubes under finite torsion, Finite Elements in Analysis and Design 112 (2016) 1–10. doi:https://doi.org/10.1016/j.finel.2015.12.003.

[70] J. Merodio, R. W. Ogden, Extension, inflation and torsion of a residually-stressed circular cylindrical tube, Continuum Mechanics and Thermodynamics 28 (1) (2016) 157–174. doi:https://doi.org/10.1007/s00161-015-0411-z.

[71] N. Nam, J. Merodio, R. Ogden, P. Vinh, The effect of initial stress on the propagation of surface waves in a layered half-space, International Journal of Solids and Structures 88-89 (2016) 88–100. doi:https://doi.org/10.1016/j.ijsolstr.2016.03.019.

[72] J. Merodio, R. Ogden, Constitutive Modelling of Solid Continua, Vol. 262 of Solid Mechanics and its Applications, Springer, Berlin, 2020. doi:https://doi.org/10.1007/978-3-030-31547-4.

[73] H. Dehghani, D. Desena-Galarza, N. Jha, J. Reinoso, J. Merodio, Bifurcation and post-bifurcation of an inflated and extended residually-stressed circular cylindrical tube with application to aneurysms initiation and propagation in arterial wall tissue, Finite Elements in Analysis and Design 161 (2019) 51–60. doi:https://doi.org/10.1016/j.finel.2019.04.004.

[74] A. Font, N. Jha, H. Dehghani, J. Reinoso, J. Merodio, Modelling of residually stressed, extended and inflated cylinders with application to aneurysms, Mechanics Research Communications 111 (2021) 103643. doi:https://doi.org/10.1016/j.mechrescom.2020.103643.

[75] T. Li, Z. Huang, Z. Suo, S. P. Lacour, S. Wagner, Stretchability of thin metal films on elastomer substrates, Applied Physics Letters 85 (16) (2004) 3435–3437. doi:https://doi.org/10.1063/1.1806275.

[76] T. Li, Z. Zhang, B. Michaux, Competing failure mechanisms of thin metal films on polymer substrates under tension, Theoretical and Applied Mechanics Letters 1 (4) (2011) 041002. doi:https://doi.org/10.1063/2.1104102.

[77] B. Bourdin, G. A. Francfort, J. J. Marigo, The variational approach to fracture, Springer Netherlands, 2008. doi:https://doi.org/10.1007/s10659-007-9107-3.

[78] J. Merodio, R. W. Ogden, J. Rodrguez, The influence of residual stress on finite deformation elastic response, International Journal of Non-Linear Mechanics 56 (2013) 43–49. doi:https://doi.org/10.1016/j.ijnonlinmec.2013.02.010.

[79] D. Balzani, J. Schröder, D. Gross, Numerical simulation of residual stresses in arterial walls, Computational Materials Science 39 (1) (2007) 117–123, proceedings of the 15th International Workshop on Computational Mechanics of Materials. doi:https://doi.org/10.1016/j.commatsci.2005.11.014.

[80] M. J. Borden, C. V. Verhoosel, M. A. Scott, T. J. R. Hughes, C. M. Landis, A phase-field description of dynamic brittle fracture, Computer Methods in Applied Mechanics and Engineering 217-220 (2012) 77–95. doi:https://doi.org/10.1016/j.cma.2012.01.008.

[81] H. Amor, J. J. Marigo, C. Maurini, Regularized formulation of the variational brittle fracture with unilateral contact: Numerical experiments, Journal of the Mechanics and Physics of Solids 57 (8) (2009) 1209–1229. doi:https://doi.org/10.1016/j.jmps.2009.04.011.

[82] R. Ostwald, E. Kuhl, A. Menzel, On the implementation of finite deformation gradient-enhanced damage models, Computational Mechanics 64 (3) (2019) 847–877. doi:https://doi.org/10.1007/s00466-019-01684-5.

[83] Y. Navidtehrani, C. Betegón, E. Martínez-Pañeda, A unified abaqus implementation of the phase field fracture method using only a user material subroutine, Materials 14 (8) (2021). doi:https://doi.org/10.3390/ma14081913.

[84] Y. Navidtehrani, C. Betegón, E. Martínez-Pañeda, A simple and robust abaqus implementation of the phase field fracture method, Applications in Engineering Science 6 (2021) 100050. doi:https://doi.org/10.1016/j.apples.2021.100050.

[85] C. Hortig, Local and non-local thermomechanical modeling and finite-element simulation of high-speed cutting, Ph.D. thesis (01 2010). doi:https://doi.org/10.17877/DE290R-15992.

[86] C. Miehe, L.-M. Schänzel, Phase field modeling of fracture in rubbery polymers. part i: Finite elasticity coupled with brittle failure, Journal of the Mechanics and Physics of Solids 65 (2014) 93–113. doi:https://doi.org/10.1016/j.jmps.2013.06.007.

[87] A. Hansen-Dörr, Phase field modelling and simulation of interface failure, Ph.D. thesis (07 2017). doi:https://doi.org/10.13140/RG.2.2.33904.35847.

[88] D. Desena-Galarza, H. Dehghani, N. Jha, J. Reinoso, J. Merodio, Computational bifurcation analysis for hyperelastic residually stressed tubes under combined inflation and extension and aneurysms in arterial tissue, Finite Elements in Analysis and Design 197 (2021) 103636. doi:https://doi.org/10.1016/j.finel.2021.103636.

Appendix A. Additional benchmark example

Further verification simulations are carried out on a square single-notched plate, whose dimensions are shown in Fig. A1(a). The discretization of the plate has been performed using 10000 elements for these series of examples with a common element size of $h = 2.5$ mm, see Fig. A1(b). The mechanical properties can be found in Tab. A1. These computations have been carried out with the exclusive consideration of hyper-viscoelastic effects for verification purposes using a staggered solution scheme. Regarding the boundary conditions of the 2-D model: the bottommost surface is fixed along the Y-direction, with the right corner also being in X-direction; and the topmost surface is submitted to a monotonically increasing vertical displacement.

A parametric study has been done to study the rate-dependency of phase field approach. Therefore, a set of relaxation times $\tau = [0.05, 0.1, 0.2]$ h and displacement rates v $= [5, 10, 20]$ mm/h are applied.

The phase field isocontour evolution at the crack initiation and propagation is shown in Figs. A1(c)-A1(d). The crack starts at the notch tip and propagates straight towards the end of the notch. This finding agrees with what is found in similar cases in viscoelastic
phase field fracture like [51] and with alternative phase field models without including viscoelastic effects [24, 34].

The reaction forces comparing the tests at different relaxation times with v $= 10$ mm/h (Fig. A2) and at different displacement rates with $\tau = 0.1$ h (Fig. A3) show
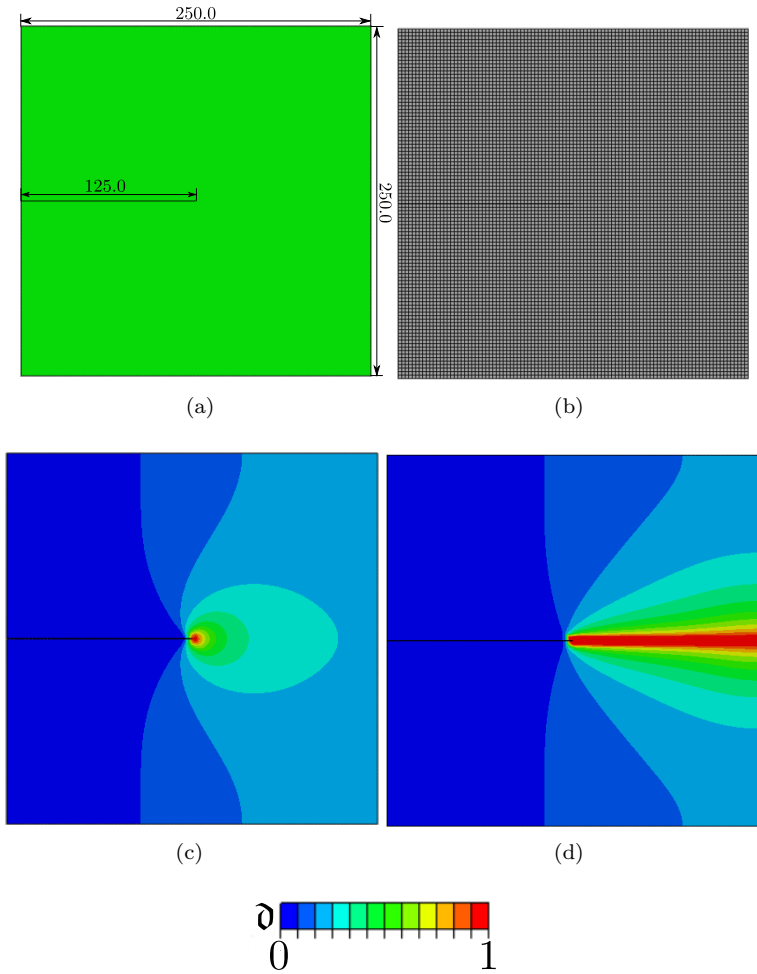
Figure A1. (a) Dimensions in mm, (b) mesh (c) and phase field isocontour for Mode I crack initiation and d) propagation of the single edge notched plate.

the clear effect of the viscosity on the specimen response. Analyzing these plots, it can be seen that for higher relaxation time, the peak force increases but the ultimate displacement becomes lower. Related to the velocity, both the final displacement and maximum force increase along with the increasing of the strain rate. The postpeak behavior shown at both of these curves, where the failure of the structure is prolonged, is in good agreement with the experimental results of [63] in a qualitative manner.
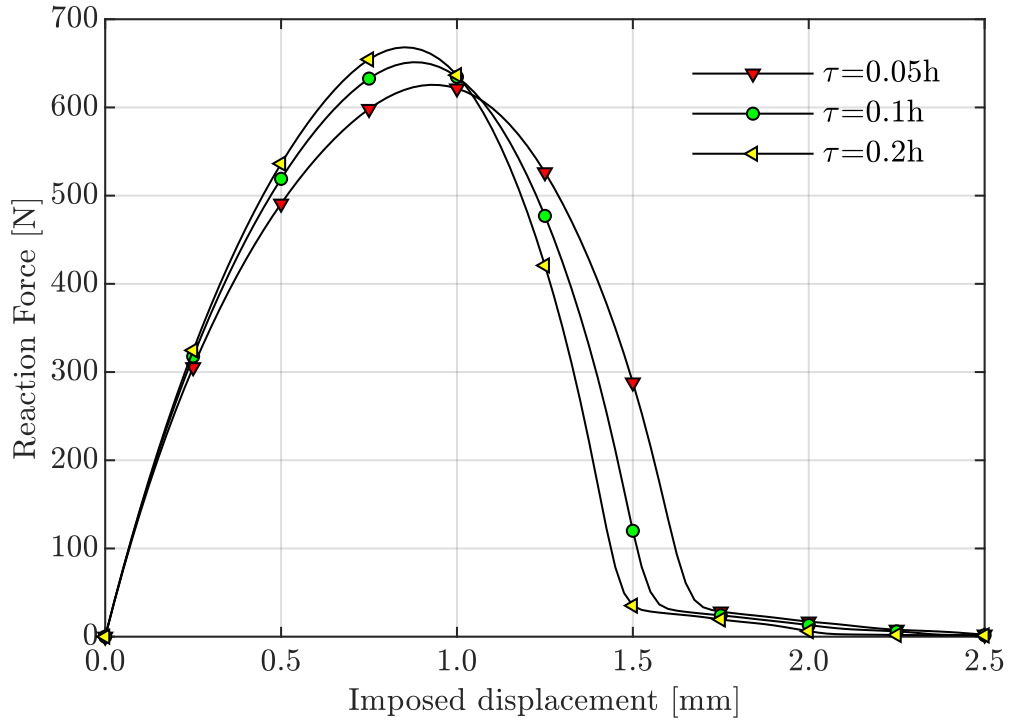
Figure A2. Load-displacement curves for tests of the single-
notched square plate with different relaxation times.

Table A1. Mechanical properties of the single edge notched square plate.

Property	Value
μ (MPa)	480
κ (MPa)	1440
μ^{visco} (MPa)	576
$\mathcal{G}_c$ (MPa $\cdot$ mm)	5
ℓ (mm)	1
f	0.5
χ	10^{-5}

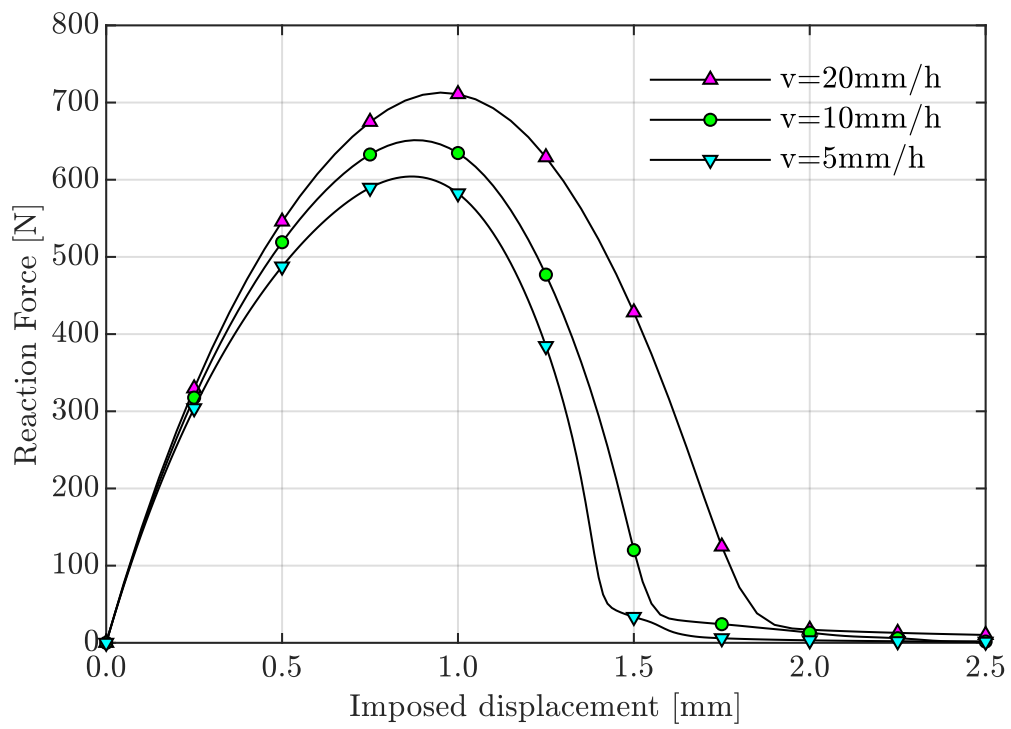**Figure A3.** Load-displacement curves for tests of the single-notched square plate with different testing rates.